

Supplementary Information for:

## Charge Transfer Mediated Triplet Excited State Formation in Donor-Acceptor-Donor BODIPY: Application for Recording of Holographic Structures in Photopolymerizable Glass

Tatsiana Mikulchyk,<sup>a</sup> Safakath Karuthedath,<sup>b</sup> Catherine S. P. De Castro,<sup>b</sup> Andrey A. Buglak,<sup>c,d</sup> Aimee Sheehan,<sup>e</sup> Aaron Wieder,<sup>e</sup> Frédéric Laquai,<sup>b</sup> Izabela Naydenova<sup>a</sup> and Mikhail A. Filatov<sup>e\*</sup>

<sup>a</sup> Centre for Industrial and Engineering Optics, School of Physics and Clinical and Optometric Sciences, College of Science and Health, Technological University Dublin, City Campus, Grangegorman, Dublin 7, Ireland

<sup>b</sup> King Abdullah University of Science and Technology (KAUST), KAUST Solar Center (KSC), Physical Sciences and Engineering Division (PSE), Material Science and Engineering Program (MSE), Thuwal 23955-6900, Kingdom of Saudi Arabia

<sup>c</sup> Faculty of Physics, Saint-Petersburg State University, University Emb. 7-9, 199034 St. Petersburg, Russia

<sup>d</sup> Institute of Physics, Department of Quantum Electronics and Radiospectroscopy, Kazan Federal University, Kremlevskaya 18, Kazan, 420008, Russian

<sup>e</sup> School of Chemical and Pharmaceutical Sciences, Technological University Dublin, City Campus, Grangegorman, Dublin 7, Ireland

E-mail: [mikhail.filatov@tudublin.ie](mailto:mikhail.filatov@tudublin.ie)

### Table of Contents

<b>1. General procedures</b> .....	2
<b>2. Synthetic procedures and characterization</b> .....	3
<b>3. NMR and mass spectroscopy</b> .....	6
<b>4. UV-Vis absorption and steady-state emission spectroscopy</b> .....	16
<b>5. Time-resolved emission spectroscopy</b> .....	18
<b>6. Computational details</b> .....	19
<b>7. Singlet oxygen generation quantum yields measurements</b> .....	23
<b>8. Transient absorption spectroscopy</b> .....	24
<b>9. Photopolymerizable glass preparation and holographic recording</b> .....	29
<b>10. References</b> .....	33

## 1. General procedures

UV-Vis absorption spectra were recorded in solutions using a PerkinElmer Lambda 900 UV/VIS/NIR Spectrometer (1 cm path length quartz cell). Fluorescence and excitation spectra were measured using a PerkinElmer LS 55 Luminescence Spectrometer. Emission quantum yields of the compounds were measured relative to the fluorescence of Rhodamine 6G in ethanol ( $\Phi_{em} = 0.95$ ).<sup>1</sup> Sample concentrations were chosen to obtain an absorbance of 0.03-0.07, at least three measurements were performed for each sample.

Time-correlated single photon counting (TCSPC) measurements were performed in a modified microscope (Olympus IX71).<sup>2</sup> The excitation source is 447 nm picosecond pulsed laser (70 ps, 100 kHz to 100 MHz variable repetition rate, DeltaDiode, HORIBA) that is passed through a 50  $\mu$ m pinhole to clean the laser output mode. The beam is directed to the back-illumination port of the microscope and focused into the sample with a 10  $\times$  0.4 N.A. air microscope objective (Olympus). The solution in 1 mm cuvette is mounted horizontally on the Physik Instrumente (PI) scanning stage. Laser excitation intensity is controlled with a set of neutral density filters (ThorLabs). The emitted light was filtered with a longpass filter 470 nm to eliminate scattered laser light and appropriate bandpass filters to select emission wavelength. The filtered signal was recollimated and sent into two avalanche photodiodes (APDs, PDM series, Micro Photon Devices) placed in a Hanbury–Brown–Twiss arrangement with a 50/50 beam splitter. Time-tagged TCSPC data was collected using HydraHarp 400 controller (PicoQuant). All the lifetime fittings were performed at posteriori in Origin 2021.

NMR spectra were recorded on a Bruker Avance II 400 MHz or a Bruker Avance III 500 MHz spectrometer. Accurate mass measurements (HRMS) were made on a hybrid quadrupole-time-of-flight mass spectrometer Bruker micrOTOF-QII at the “Center de Spectrométrie de Masse”, University of Lyon. Solutions in CHCl<sub>3</sub>/methanol (1:1, v/v) were used for the analyses. The analyses were performed in positive mode using full scan MS with a mass range from 50 to 2000 Da at an acquisition rate of 1 Hz. Melting points were measured using an automated melting point meter SMP10 (Stuart) and are uncorrected.

## 2. Synthetic procedures and characterization

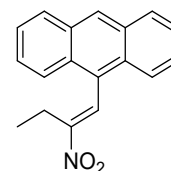
The handling of all air/water sensitive materials was carried out using standard high vacuum techniques. Tetrahydrofuran and dichloromethane were distilled from  $\text{LiAlH}_4$  and  $\text{CaH}_2$ , respectively. All other solvents were used as commercially supplied. Analytical thin layer chromatography was performed using silica gel 60 (fluorescence indicator F254, pre-coated sheets, 0.2 mm thick, 20 cm  $\times$  20 cm; Merck) plates and visualized by UV irradiation ( $\lambda = 254$  nm). Column chromatography was carried out using Fluka Silica Gel 60 (230–400 mesh).

Anthracene-9-carbaldehyde, pyrene-1-carbaldehyde, benzaldehyde, ethyl isocyanoacetate, 1-nitropropane, 1,8-diazabicyclo[5.4.0]undec-7-ene, lithium aluminium hydride, ammonium acetate, boron trifluoride diethyl etherate and *N,N*-diisopropylethylamine were purchased from Sigma-Aldrich.

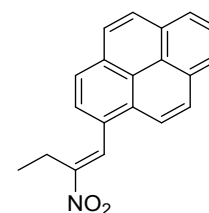
### 1.1 General procedure for the synthesis of nitroalkenes.

Aromatic aldehyde (25 mmol) was mixed with ammonium acetate (3.85 g, 50 mmol) in 1-nitropropane (20 mL). This solution was then heated at around 115 °C until the starting material's spot disappeared on the TLC (4–8 h). The reaction mixture was cooled to room temperature and then to -20 °C. The resulting solid was filtered and recrystallized from ethanol to give pure products.

Compound **1a**. Yellow crystalline solid, m.p. 162–165 °C, 59 % yield.  $^1\text{H}$  NMR (400 MHz,  $\text{CDCl}_3$ )  $\delta$  8.59 (d,  $J = 0.6$  Hz, 1H), 8.52 (s, 1H), 8.10 – 8.01 (m, 2H), 7.97 – 7.90 (m, 2H), 7.57 – 7.50 (m, 4H), 2.39 (q,  $J = 7.4$  Hz, 2H), 0.92 (t,  $J = 7.4$  Hz, 3H).  $^{13}\text{C}$  NMR (100 MHz,  $\text{CDCl}_3$ )  $\delta$  156.87, 131.31, 130.92, 129.14, 128.96, 128.51, 126.83, 125.94, 125.77, 125.10, 21.55, 11.80.



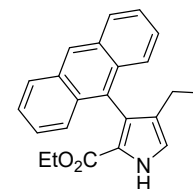
Compound **1b**. Yellow crystalline solid, m.p. 128–130 °C, 63 % yield.  $^1\text{H}$  NMR (400 MHz,  $\text{CDCl}_3$ )  $\delta$  8.86 (s, 1H), 8.26 (d,  $J = 7.7$  Hz, 2H), 8.23 – 8.05 (m, 6H), 7.94 (dd,  $J = 8.0, 0.6$  Hz, 1H), 2.86 (q,  $J = 7.4$  Hz, 2H), 1.28 (t,  $J = 7.4$  Hz, 3H).  $^{13}\text{C}$  NMR (100 MHz,  $\text{CDCl}_3$ )  $\delta$  154.86, 132.39, 132.21, 131.29, 130.82, 129.78, 128.91, 128.82, 127.28, 126.58, 126.27, 126.19, 126.12, 124.75, 124.47, 123.34, 21.10, 12.82.



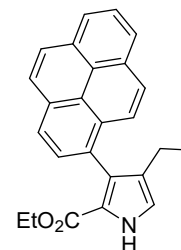
### 1.2 General procedure for the Barton-Zard reaction.

1,8-diazabicyclo[5.4.0]undec-7-ene (2.74 g, 18 mmol) was added dropwise to a mixture of corresponding nitroalkene (15 mmol) ethyl isocyanoacetate (0.702 g, 15 mmol) in THF (30 mL). The mixture was left to stir under inert atmosphere overnight, then was evaporated in vacuum. The residue was dissolved in dichloromethane (5 mL) and the solution was loaded on short silica gel column (5 cm) which was then washed with 150 mL of dichloromethane. The resulting solution was concentrated in vacuum and the obtained residue was recrystallized from methanol (**2a**) or acetone – diethyl ether mixture (**2b**) to give pure products.

Compound **2a**. Yellow crystalline solid, m.p. 164–166 °C, 78 % yield.  $^1\text{H}$  NMR (400 MHz,  $\text{CDCl}_3$ )  $\delta$  9.37 (brs, 1H), 8.46 (s, 1H), 8.04 – 8.01 (m, 2H), 7.73 – 7.68 (m, 2H), 7.46 – 7.40 (m, 2H), 7.36 – 7.30 (m, 2H), 7.05 (dt,  $J = 3.0, 0.7$  Hz, 1H), 3.72 – 3.65 (m, 2H), 2.09 (qd,  $J = 7.5, 0.7$  Hz, 2H), 0.90 (t,  $J = 7.5$  Hz, 3H), 0.31 (t,  $J = 7.1$  Hz, 3H).  $^{13}\text{C}$  NMR (100 MHz,  $\text{CDCl}_3$ )  $\delta$  161.54, 131.49, 131.02, 130.79, 129.72, 128.41, 127.00, 126.22, 126.03, 125.08, 124.98, 121.49, 119.72, 59.62, 18.81, 14.66, 13.19.



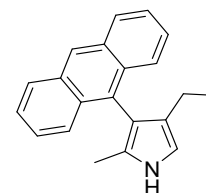
Compound **2b**. Yellow crystalline solid, m.p. 163-165 °C, 66 % yield. <sup>1</sup>H NMR (400 MHz, CDCl<sub>3</sub>) δ 9.24 (brs, 1H), 8.21 – 8.06 (m, 5H), 8.01 – 7.86 (m, 4H), 6.97 (d, *J* = 3.0 Hz, 1H), 3.92 – 3.83 (m, 2H), 2.32 – 2.19 (m, 2H), 0.96 (t, *J* = 7.6 Hz, 3H), 0.61 (t, *J* = 7.1 Hz, 3H). <sup>13</sup>C NMR (100 MHz, CDCl<sub>3</sub>) δ 161.46, 131.51, 131.19, 130.54, 130.00, 129.18, 128.74, 128.62, 127.67, 127.14, 127.01, 126.07, 125.86, 124.99, 124.94, 124.85, 124.77, 124.25, 120.71, 119.45, 59.88, 18.83, 14.92, 13.76.



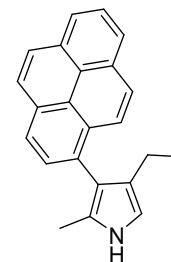
### 1.3 General procedure for the reduction of ethoxycarbonylpyrroles with LiAlH<sub>4</sub>.

LiAlH<sub>4</sub> (0.456 g, 12 mmol) was added to dry THF (30 mL) under nitrogen, the mixture was stirred and cooled to 0°C. Corresponding ethoxycarbonyl pyrrole (3 mmol) was dissolved in dry THF (10 mL) and the solution was added dropwise into the reaction flask. The mixture was heated under reflux 6 h, cooled to room and then to 0°C. Aqueous solution of NaOH (10%, 5 mL) was added slowly to quench the residual LiAlH<sub>4</sub>. The resulting mixture was filtered through a short layer of silica (5 cm) which was then washed THF (20 mL). The solvent was removed in vacuum to give the target products which were used without additional purification.

Compound **3a**. Brownish semisolid froth, 99 % yield. <sup>1</sup>H NMR (400 MHz, CDCl<sub>3</sub>) δ 8.44 (brs, 1H), 8.06 – 8.00 (m, 2H), 7.96 (s, 1H), 7.84 (ddd, *J* = 8.7, 2.0, 0.9 Hz, 2H), 7.48 – 7.41 (m, 2H), 7.39 – 7.32 (m, 2H), 6.71 – 6.69 (m, 1H), 2.07 (qt, *J* = 3.4, 1.7 Hz, 2H), 1.89 (s, 3H), 0.85 (t, *J* = 7.5 Hz, 3H). <sup>13</sup>C NMR (100 MHz, CDCl<sub>3</sub>) δ 131.95, 131.58, 131.52, 128.35, 127.69, 127.43, 126.33, 125.77, 124.93, 124.88, 116.27, 112.10, 19.23, 14.60, 11.80.



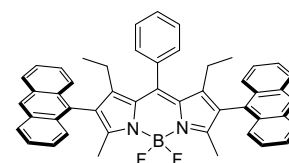
Compound **3b**. Dark-yellow semisolid froth, 93 % yield. <sup>1</sup>H NMR (500 MHz, CDCl<sub>3</sub>) δ 8.25 – 7.88 (m, 10H), 6.68 (br. s, 1H), 2.38 (ddt, *J* = 22.7, 15.3, 7.6 Hz, 2H), 2.12 (s, 3H), 1.01 (t, *J* = 7.5 Hz, 3H). <sup>13</sup>C NMR (126 MHz, CDCl<sub>3</sub>) δ 131.49, 131.20, 130.19, 130.07, 129.17, 127.89, 127.54, 126.90, 126.85, 126.45, 126.40, 125.81, 125.02, 124.73, 124.61, 124.52, 123.73, 112.32, 19.31, 14.82, 12.00.



### 1.4 General procedure for BODIPY synthesis.

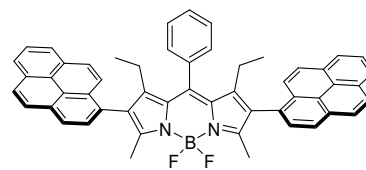
Corresponding pyrrole (3 mmol) and benzaldehyde (1.5 mmol) were mixed in anhydrous dichloromethane (30 mL) and the solution was degassed by bubbling nitrogen for 10 min. Trifluoroacetic acid (10 μL, 0.13 mmol) was added and the reaction mixture was stirred for 12 h under inert atmosphere. 2,3-Dichloro-5,6-dicyano-1,4-benzoquinone (DDQ) (0.3405 g, 1.5 mmol) was added and the mixture was stirred for another 20 min. The reaction mixture was then transferred into a separating funnel and washed with water (2 × 30 mL). Organic phase was separated, dried over Na<sub>2</sub>SO<sub>4</sub> and evaporated to dryness in vacuum. The solid residue was re-dissolved in anhydrous dichloromethane (30 mL), then N-ethyl-diisopropylamine (0.87 mL, 5 mmol) and BF<sub>3</sub>•Et<sub>2</sub>O (0.62 mL, 5 mmol) were added under stirring. The reaction mixture was stirred for 1 h under inert atmosphere. The reaction mixture was transferred into a separation funnel and washed with water (2 × 30 mL). The organic phases were combined, dried over Na<sub>2</sub>SO<sub>4</sub> and evaporated to dryness in vacuum. The crude products were purified by silica gel column chromatography hexane – dichloromethane mixture (1:1 v/v) as an eluent to afford analytically pure compounds.

Compound **ABA**. Orange crystalline solid, m.p. >300 °C, 36 % yield. <sup>1</sup>H NMR (400 MHz, CDCl<sub>3</sub>) δ 8.51 (s, 2H), 8.08 – 8.04 (m, 4H), 7.78 (dd, *J* = 8.6, 0.9 Hz, 4H), 7.69 – 7.66 (m, 2H), 7.51 – 7.40 (m, 11H), 2.24 (s, 6H), 1.44 – 1.34 (m, 4H), 0.25 (t, *J* = 7.4 Hz, 6H). <sup>13</sup>C NMR (100 MHz, CDCl<sub>3</sub>) δ 156.61, 149.35, 142.11, 134.49, 131.49, 131.31, 130.99, 129.47, 129.19, 128.96, 128.69, 128.16, 128.14, 127.33, 126.24, 125.94, 125.29, 19.73, 15.63, 13.19. <sup>19</sup>F NMR (376 MHz, CDCl<sub>3</sub>) δ -145.49 (dd, *J* = 64.8, 31.6 Hz). HRMS (ESI): *m/z* found 727.3073, calcd for [M+Na]<sup>+</sup>



C<sub>49</sub>H<sub>39</sub>BF<sub>2</sub>N<sub>2</sub>Na 727.3067.

Compound **PBP**. Orange crystalline solid, m.p. 262-264 °C, 23 % yield. <sup>1</sup>H NMR (500 MHz, CDCl<sub>3</sub>) δ 8.27 – 8.16 (m, 6H), 8.14 – 8.00 (m, 8H), 7.93 – 7.82 (m, 4H), 7.69 – 7.59 (m, 2H), 7.50 – 7.40 (m, 3H), 2.41 (s, 6H), 1.66 (ddd, *J* = 20.6, 13.6, 7.2 Hz, 2H), 1.49 (tt, *J* = 14.5, 7.3 Hz, 2H), 0.41 (t, *J* = 7.3 Hz, 6H). <sup>13</sup>C NMR (126 MHz, CDCl<sub>3</sub>) δ 155.98, 148.32, 142.40, 134.74, 132.39, 131.43, 131.26, 131.16, 131.09, 130.25, 129.36, 129.22, 129.21, 129.13, 129.09, 129.05, 128.77, 128.73, 128.28, 127.98, 127.75, 127.51, 126.25, 125.42, 125.34, 125.31, 125.25, 125.06, 124.89, 124.82, 19.55, 16.13, 13.56. HRMS (ESI): *m/z* found 775.3074, calcd for [M+Na]<sup>+</sup> C<sub>53</sub>H<sub>39</sub>BF<sub>2</sub>N<sub>2</sub>Na 775.3067.



### 3. NMR and mass spectroscopy

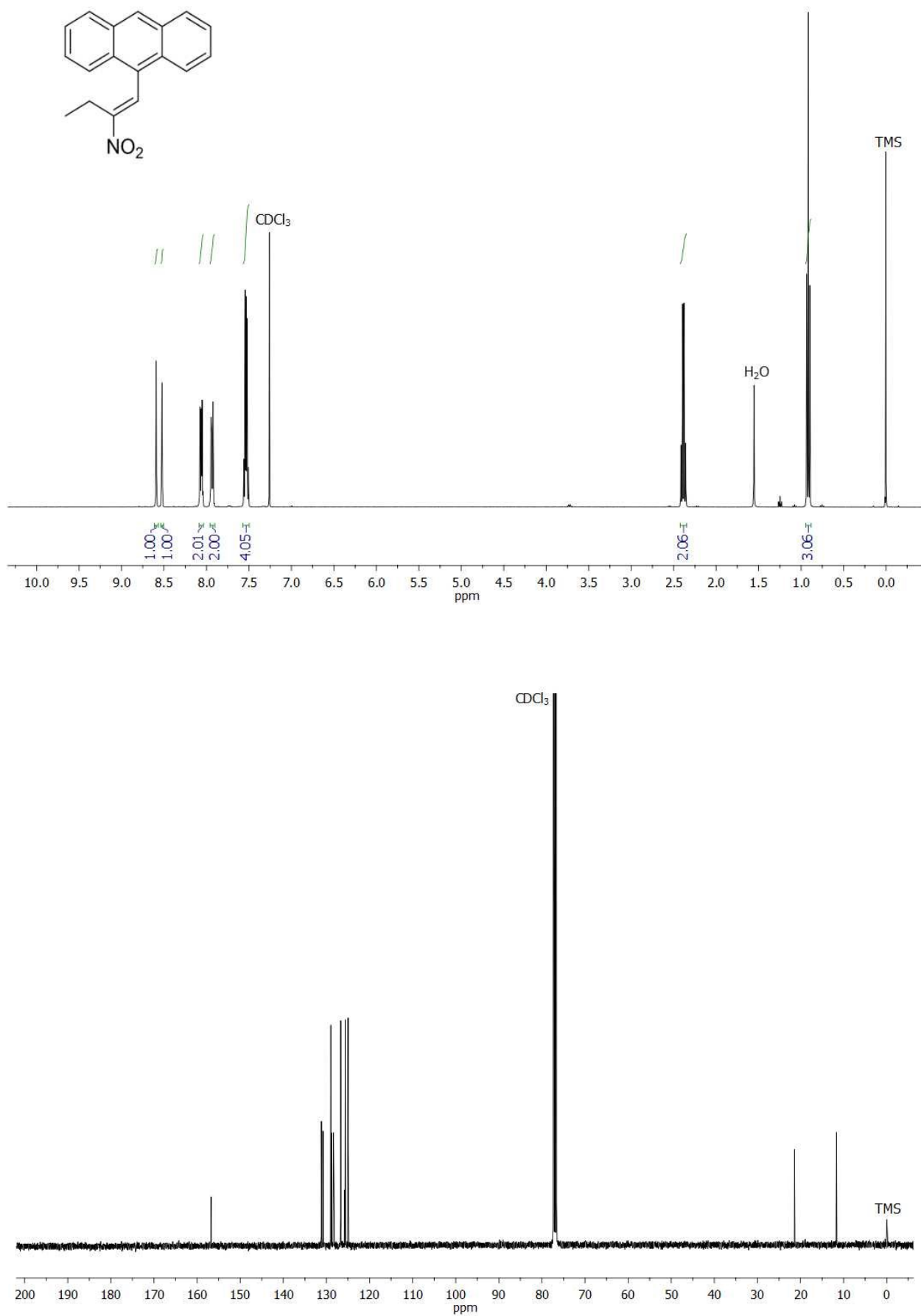


**Figure S1.**  $^1\text{H}$  and  $^{13}\text{C}$  NMR spectra of compound **1a**.

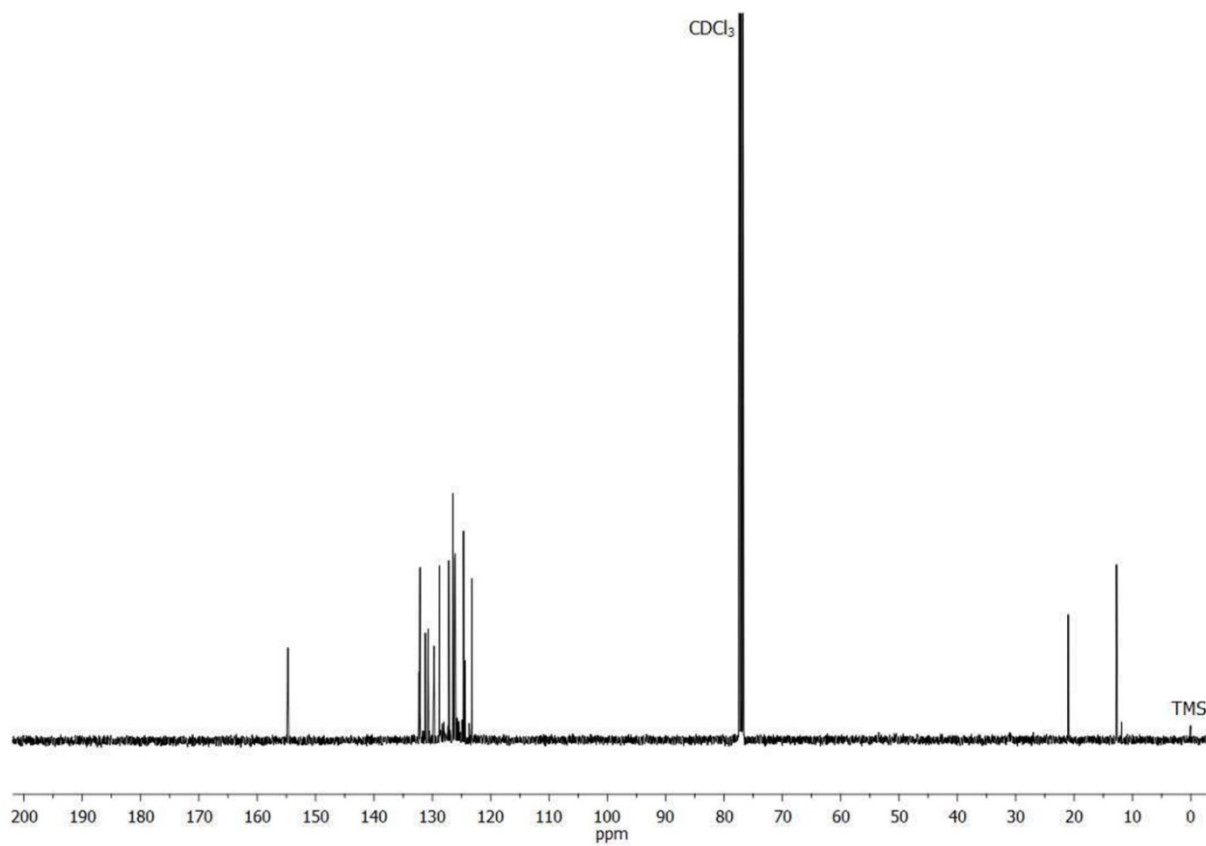
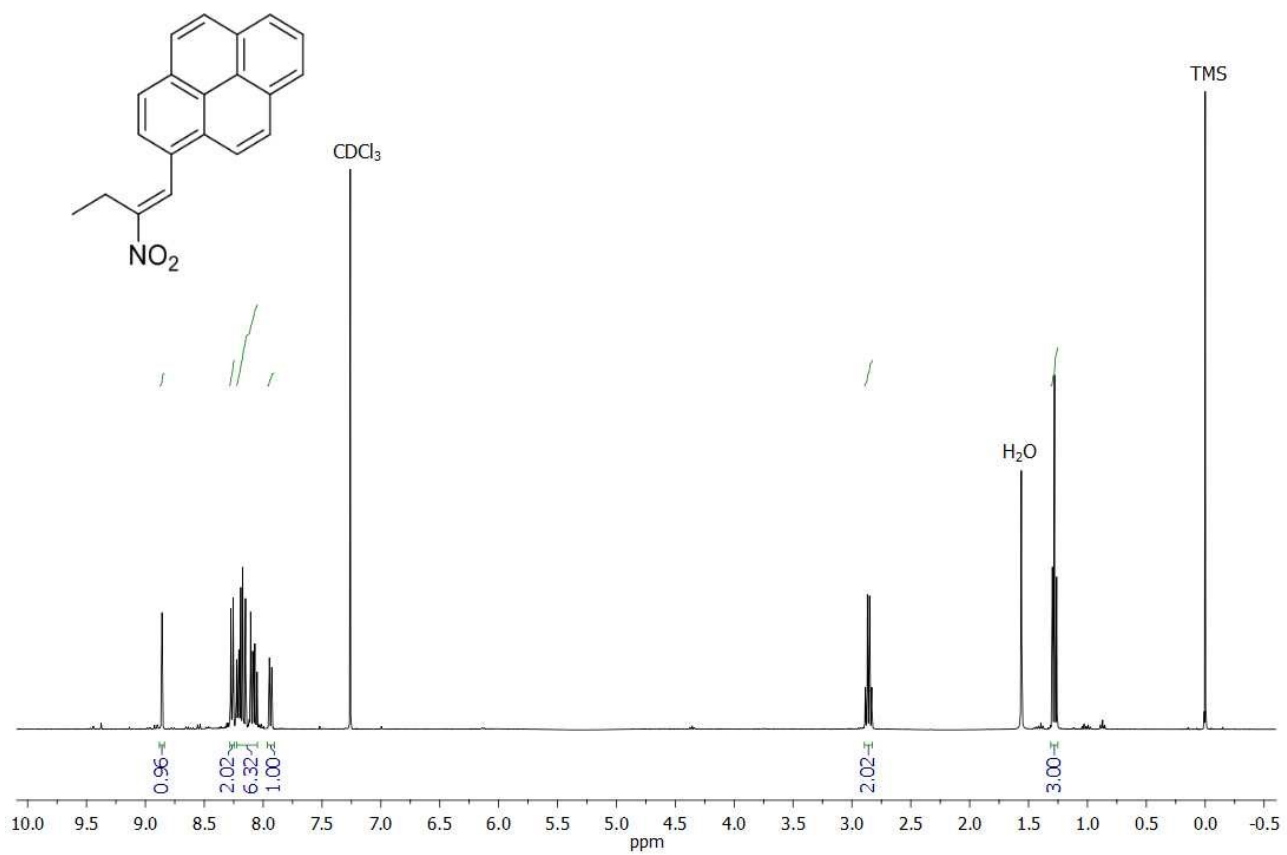


**Figure S2.** <sup>1</sup>H and <sup>13</sup>C NMR spectra of compound **1b**.

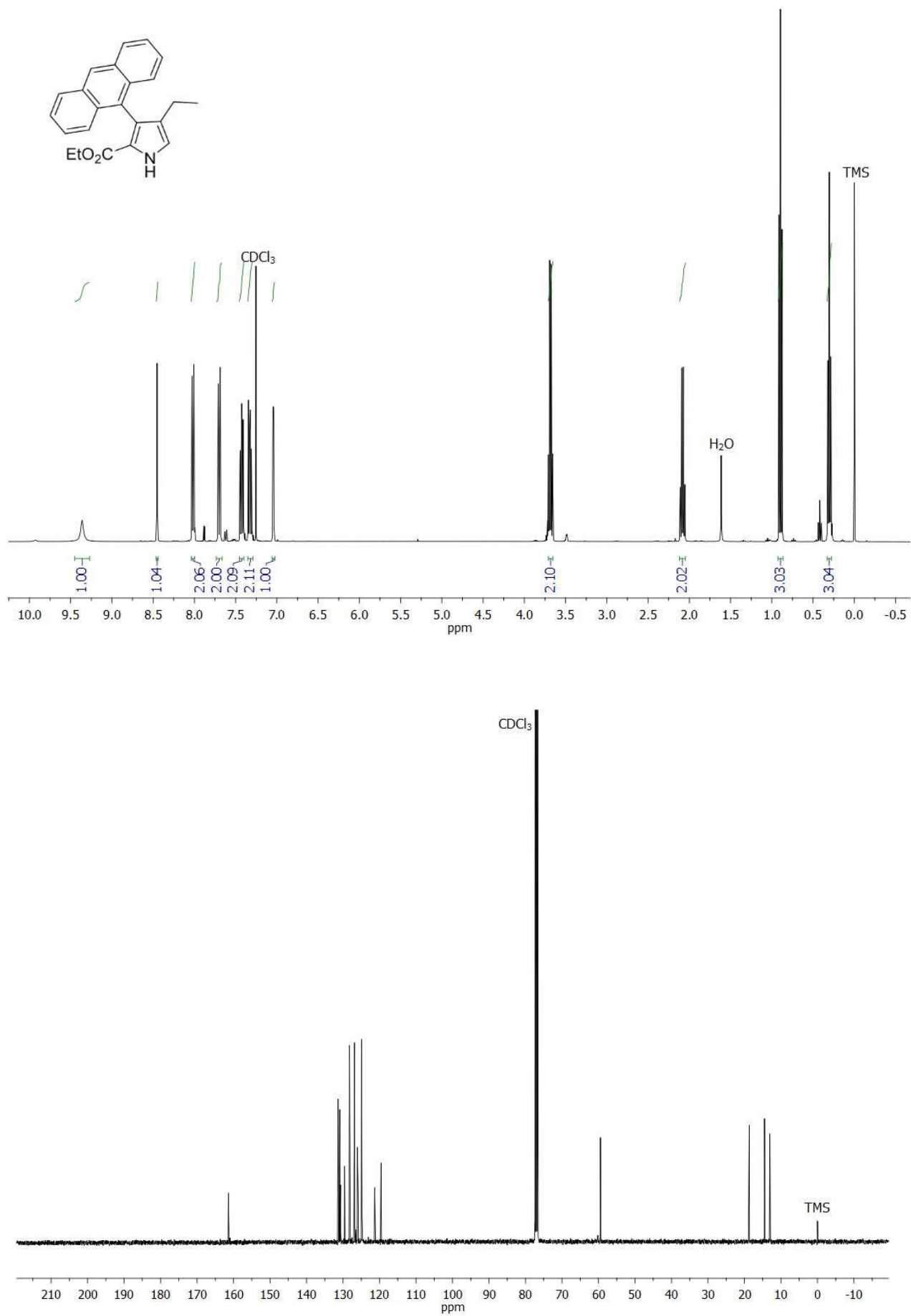


**Figure S3.**  $^1\text{H}$  and  $^{13}\text{C}$  NMR spectra of compound 2a.

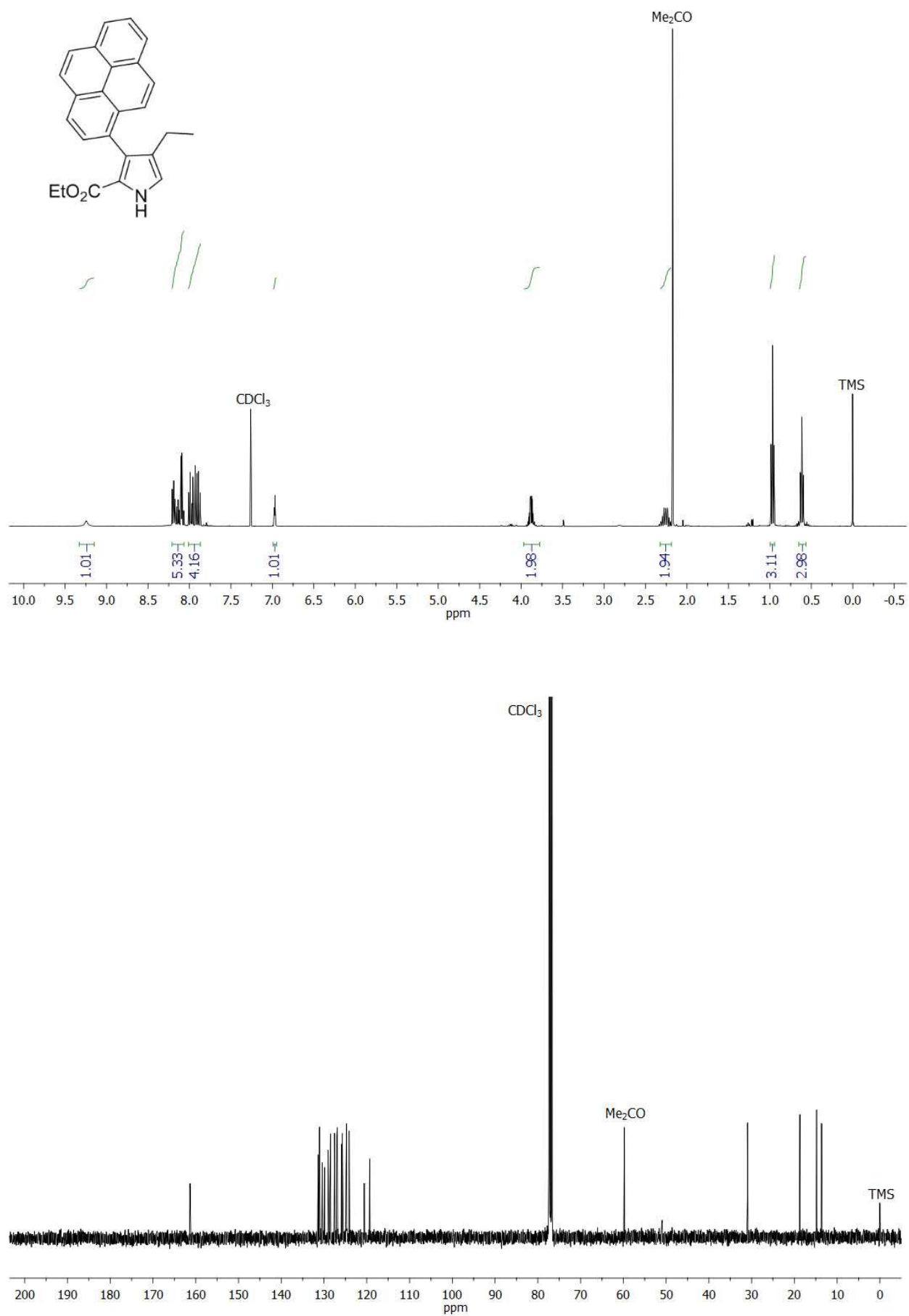


**Figure S4.**  $^1\text{H}$  and  $^{13}\text{C}$  NMR spectra of compound 2b.

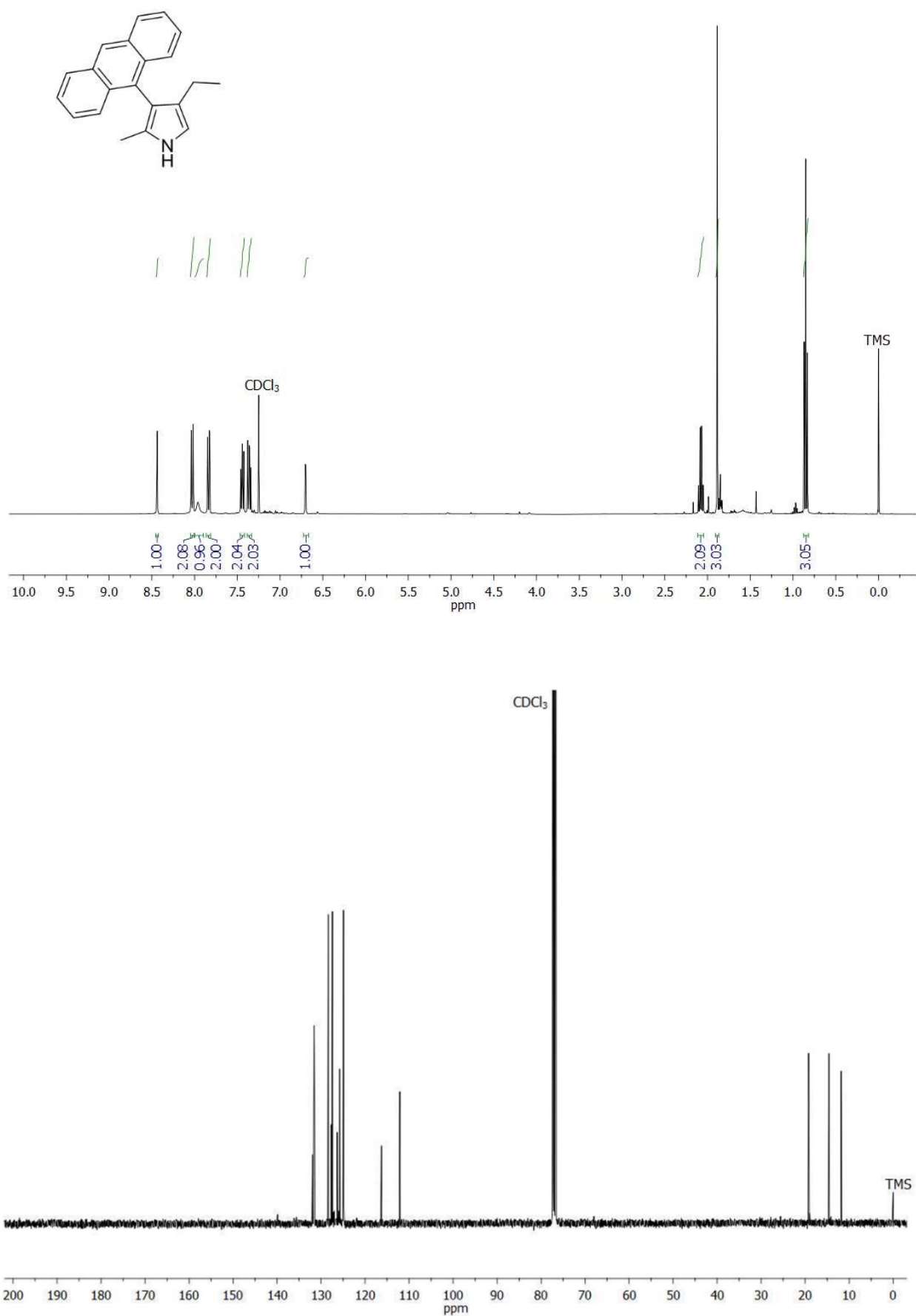
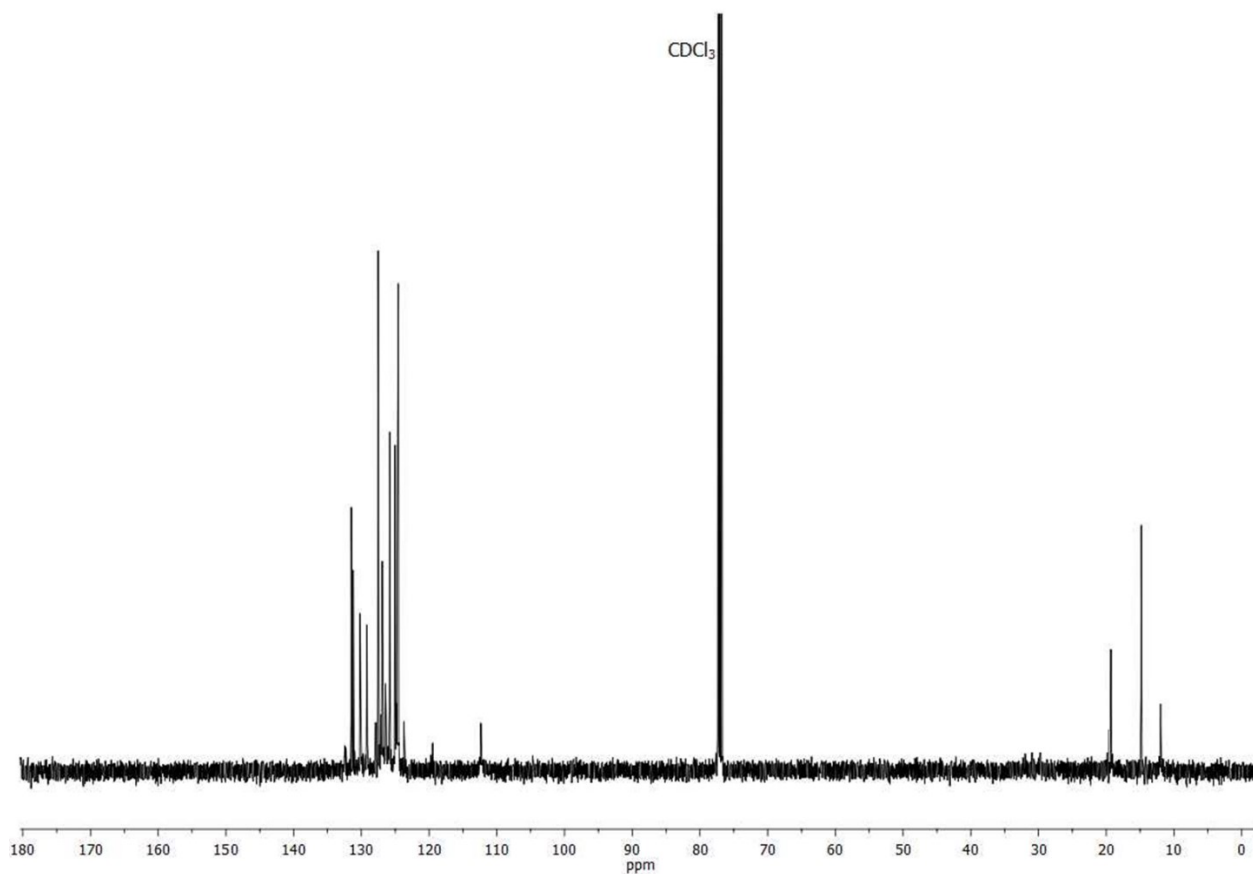
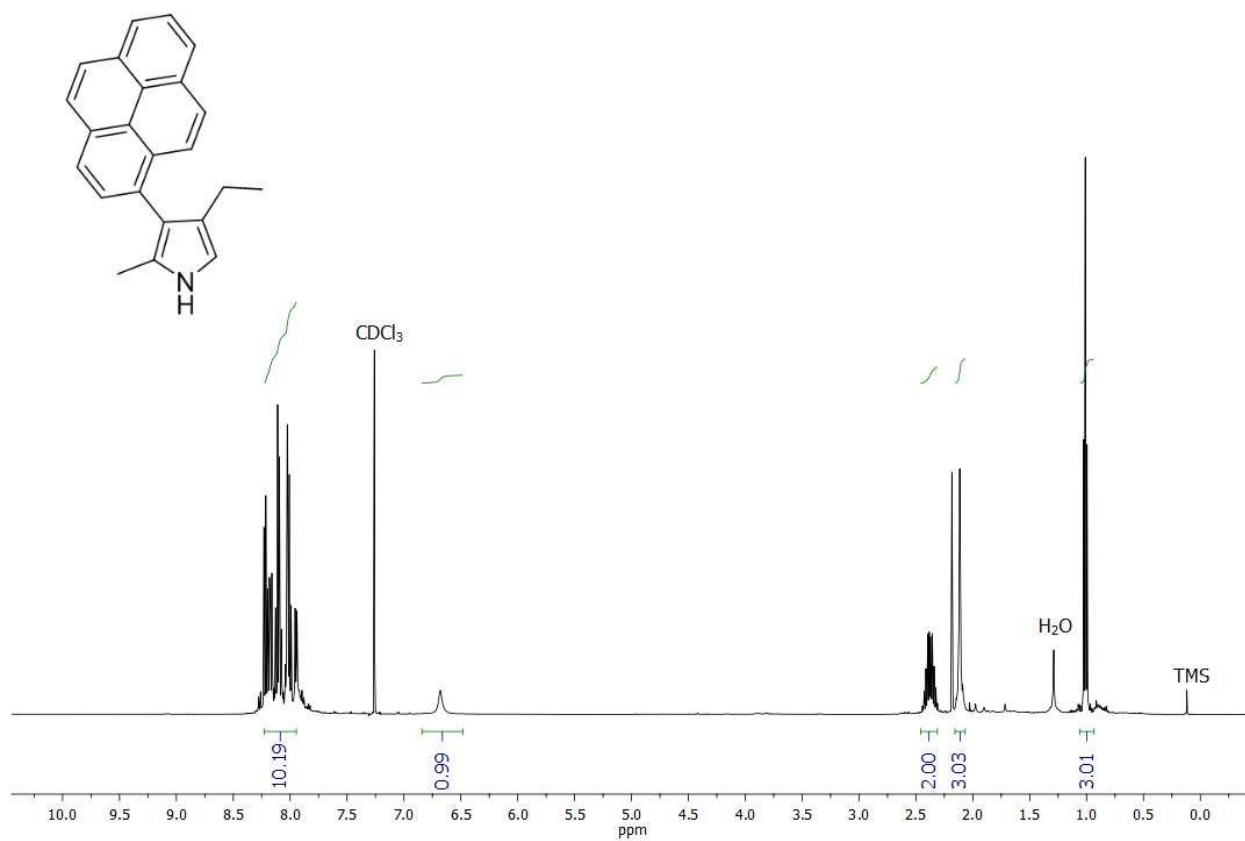
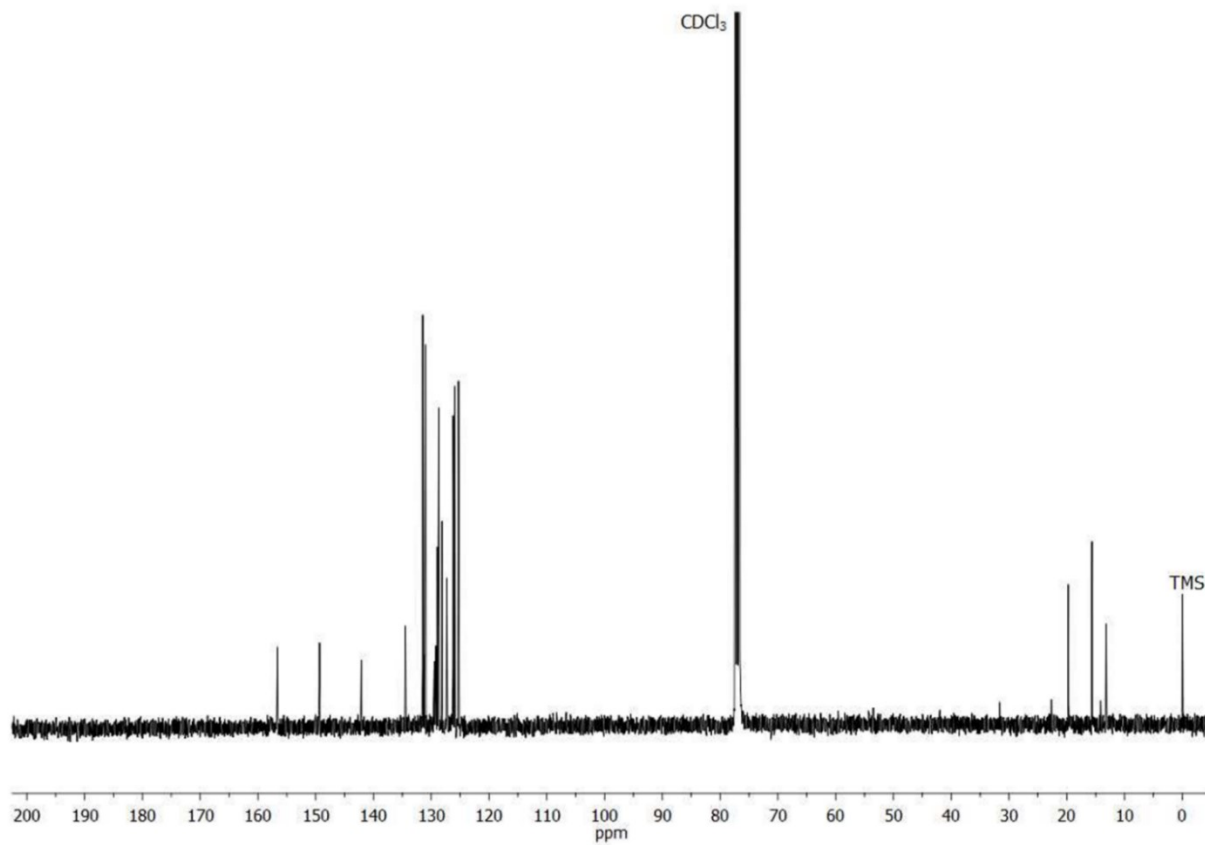
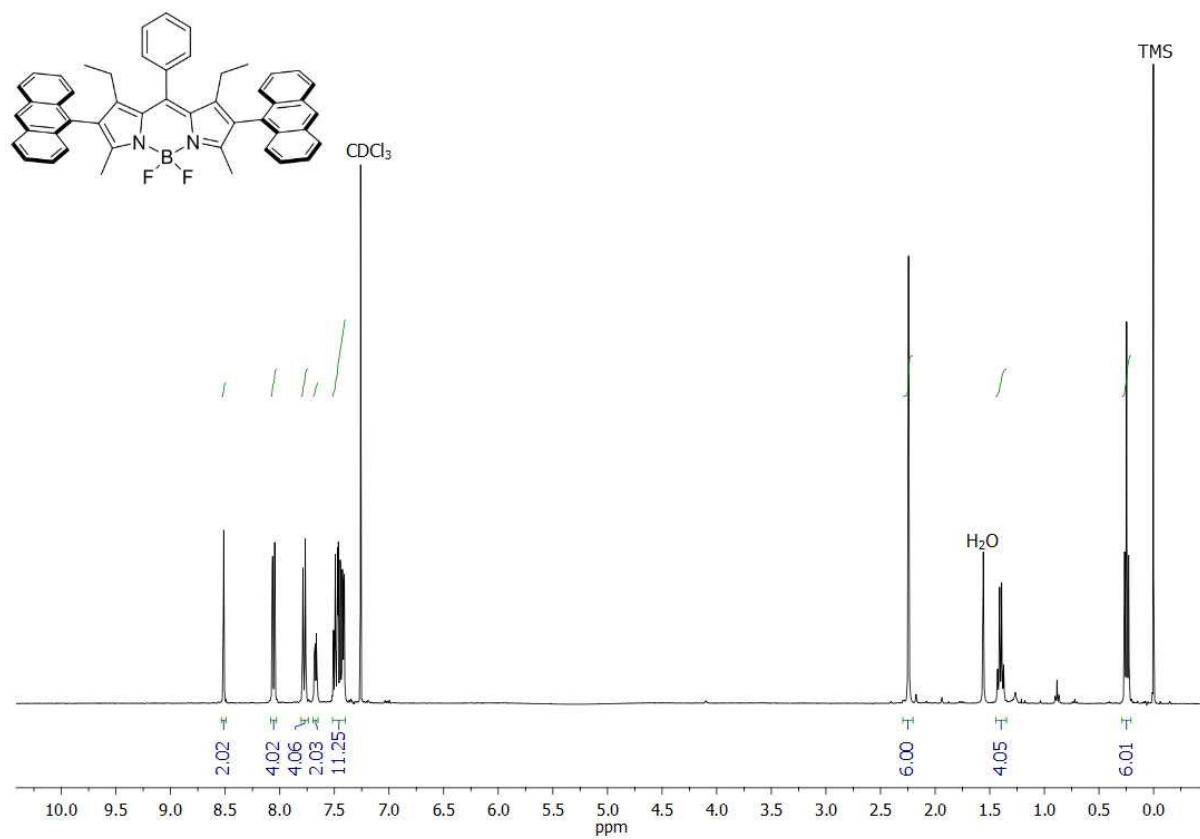


Figure S5.  $^1\text{H}$  and  $^{13}\text{C}$  NMR spectra of compound 3a.



**Figure S6.** <sup>1</sup>H and <sup>13</sup>C NMR spectra of compound **3b**.



**Figure S7.**  $^1\text{H}$  and  $^{13}\text{C}$  NMR spectra of compound ABA.

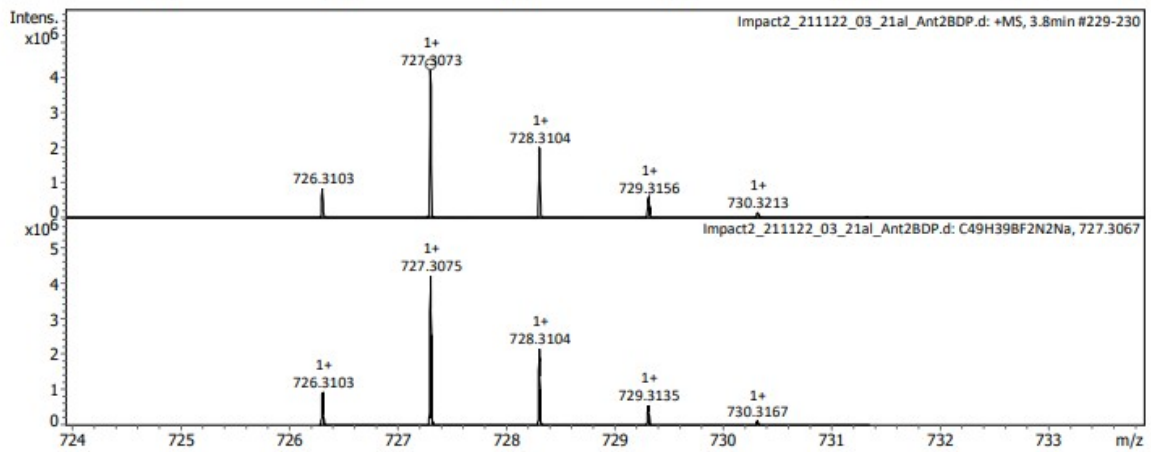
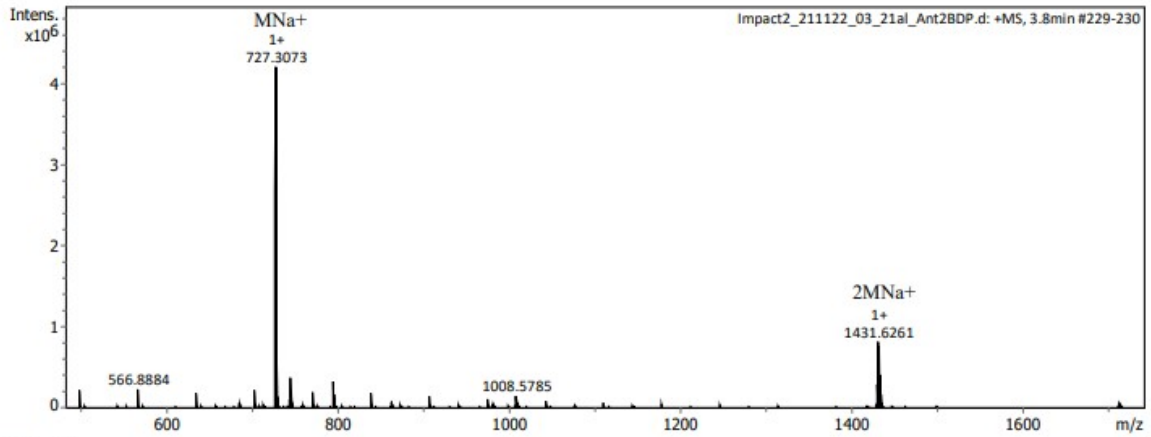
**Analysis Info**

Analysis Name Impact2\_211122\_03\_21a\_Ant2BDP.d  
Method Tune\_pos\_Standard.m  
Comment

Acquisition Date 11/22/2021 10:20:49 AM  
Instrument / Ser# impact II 1825265.1  
0081

**Acquisition Parameter**

Source Type	ESI	Ion Polarity	Positive	Set Nebulizer	0.3 Bar
Focus	Active	Set Capillary	4500 V	Set Dry Heater	200 °C
Scan Begin	20 m/z	Set End Plate Offset	-500 V	Set Dry Gas	4.0 l/min
Scan End	2500 m/z	Set Collision Cell RF	1500.0 Vpp	Set Divert Valve	Source



Meas. m/z	Ion Formula	Sum Formula	err [ppm]	mSigma	Adduct	z
727.3073	C49H39BF2N2Na	C49H39BF2N2	0.2	19.0	M+Na	1+
1431.6261	C98H78B2F4N4Na		0.5	41.2	2M+Na	1+

**Figure S8.** ESI HRMS spectrum of ABA (positive mode).

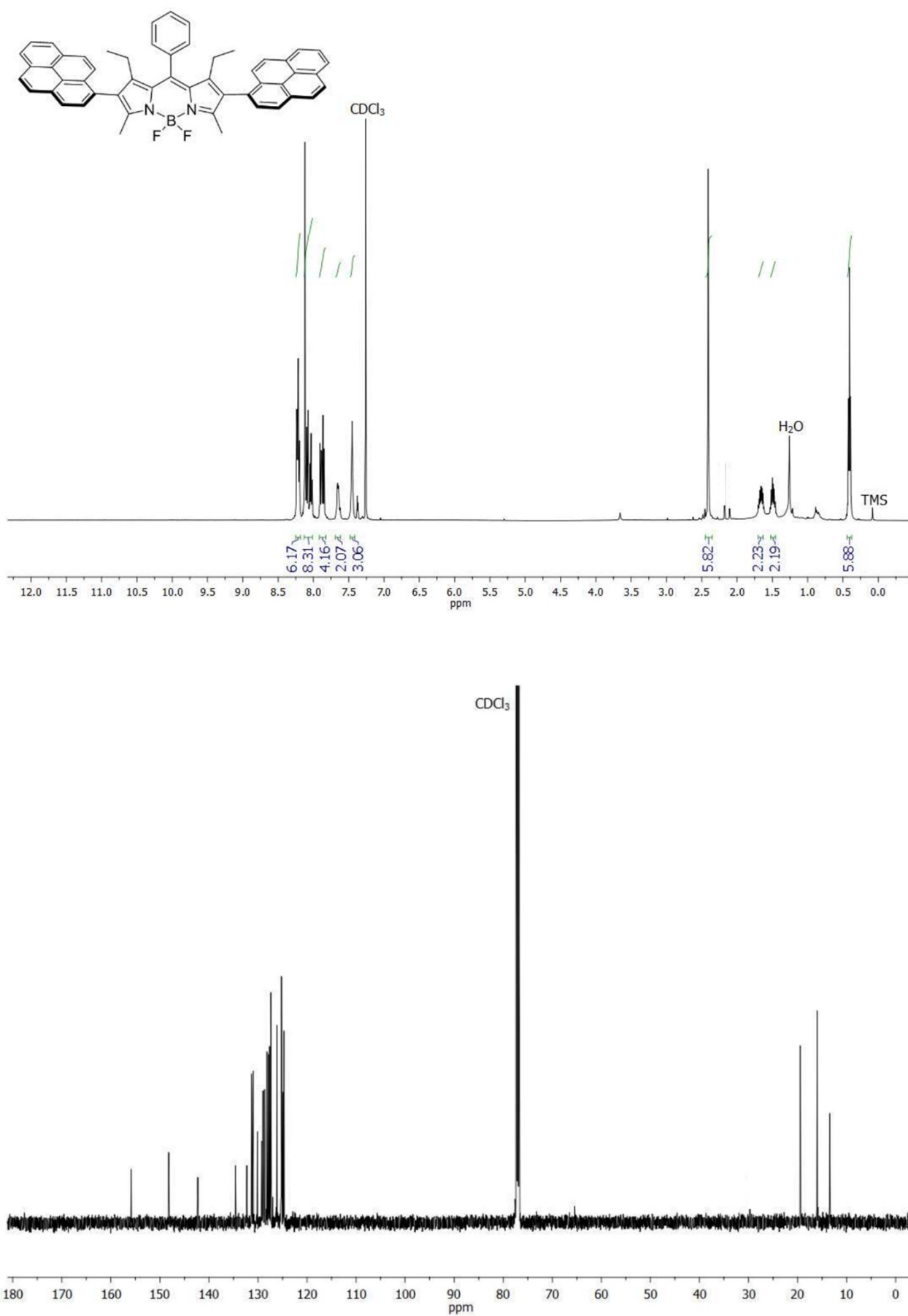


**Figure S9.**  $^1\text{H}$  and  $^{13}\text{C}$  NMR spectra of compound PBP.

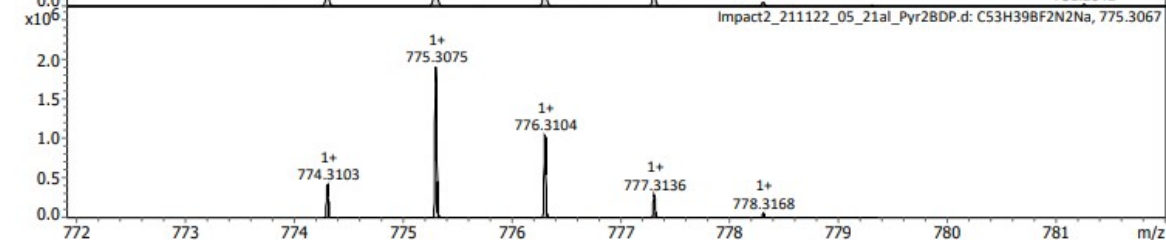
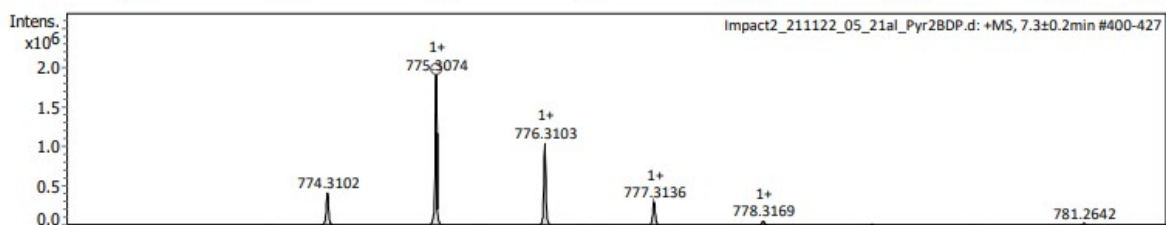
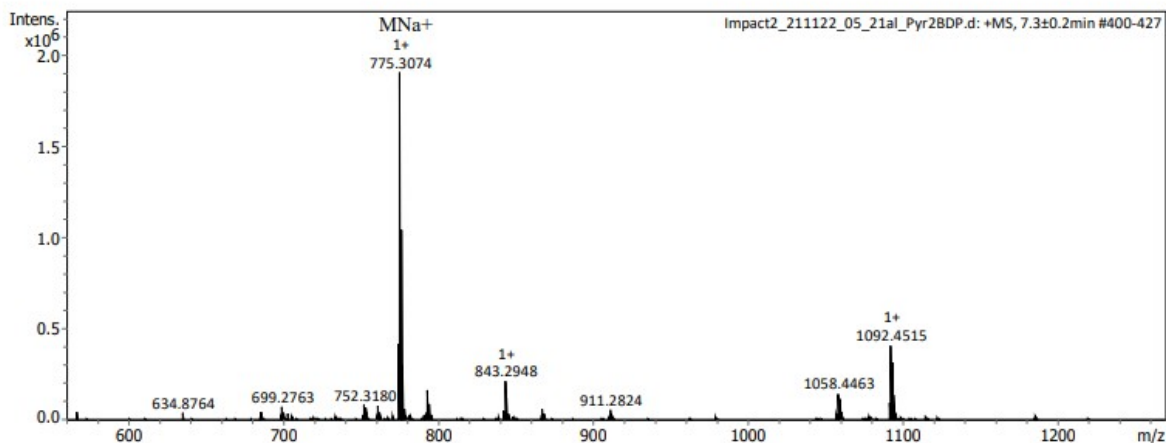
**Analysis Info**

Analysis Name Impact2\_211122\_05\_21a1\_Pyr2BDP.d  
Method Tune\_pos\_Standard.m  
Comment

Acquisition Date 11/22/2021 10:52:23 AM  
Instrument / Ser# impact II 1825265.1  
0081

**Acquisition Parameter**

Source Type	ESI	Ion Polarity	Positive	Set Nebulizer	0.3 Bar
Focus	Active	Set Capillary	4500 V	Set Dry Heater	200 °C
Scan Begin	50 m/z	Set End Plate Offset	-500 V	Set Dry Gas	4.0 l/min
Scan End	2500 m/z	Set Collision Cell RF	750.0 Vpp	Set Divert Valve	Source



Meas. m/z	Ion Formula	Sum Formula	err [ppm]	mSigma	Adduct	z
775.3074	C53H39BF2N2Na	C53H39BF2N2	0.2	2.5	M+Na	1+

**Figure S10.** ESI HRMS spectrum of **PBP** (positive mode).

## 4. UV-Vis absorption and steady-state emission spectroscopy

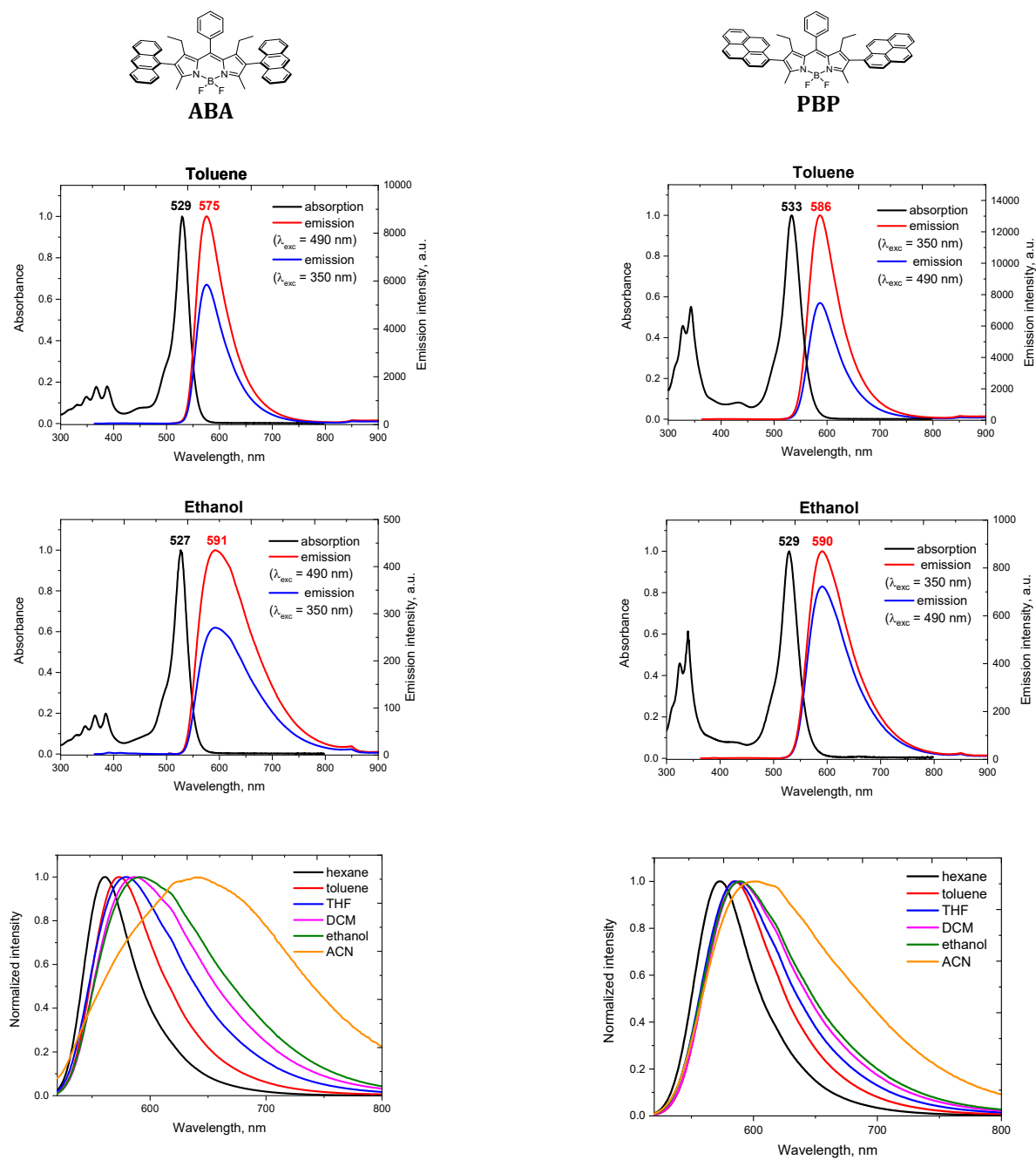


**Figure S11.** Absorption and emission spectra of **ABA** and **PBP** in different solvents.

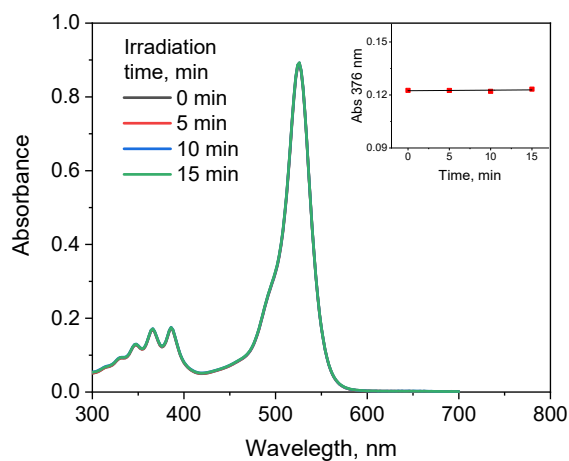


**Figure S12.** Absorption of **ABA** in toluene upon irradiation with 514 nm laser ( $20 \text{ mW cm}^{-2}$ ). Inset: dependence of absorbance at 376 nm on the irradiation time.

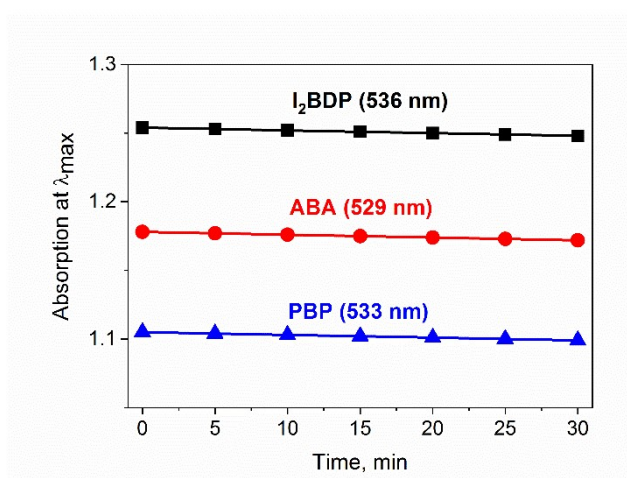


**Figure S13.** Comparison of photostability of **I<sub>2</sub>BDP**, **ABA** and **PBP**. The change of the absorption at  $\lambda_{\text{max}}$  in air-saturated toluene upon continuous laser illumination ( $514 \text{ nm}$ ,  $20 \text{ mW cm}^{-2}$ ).

## 5. Time-resolved emission spectroscopy

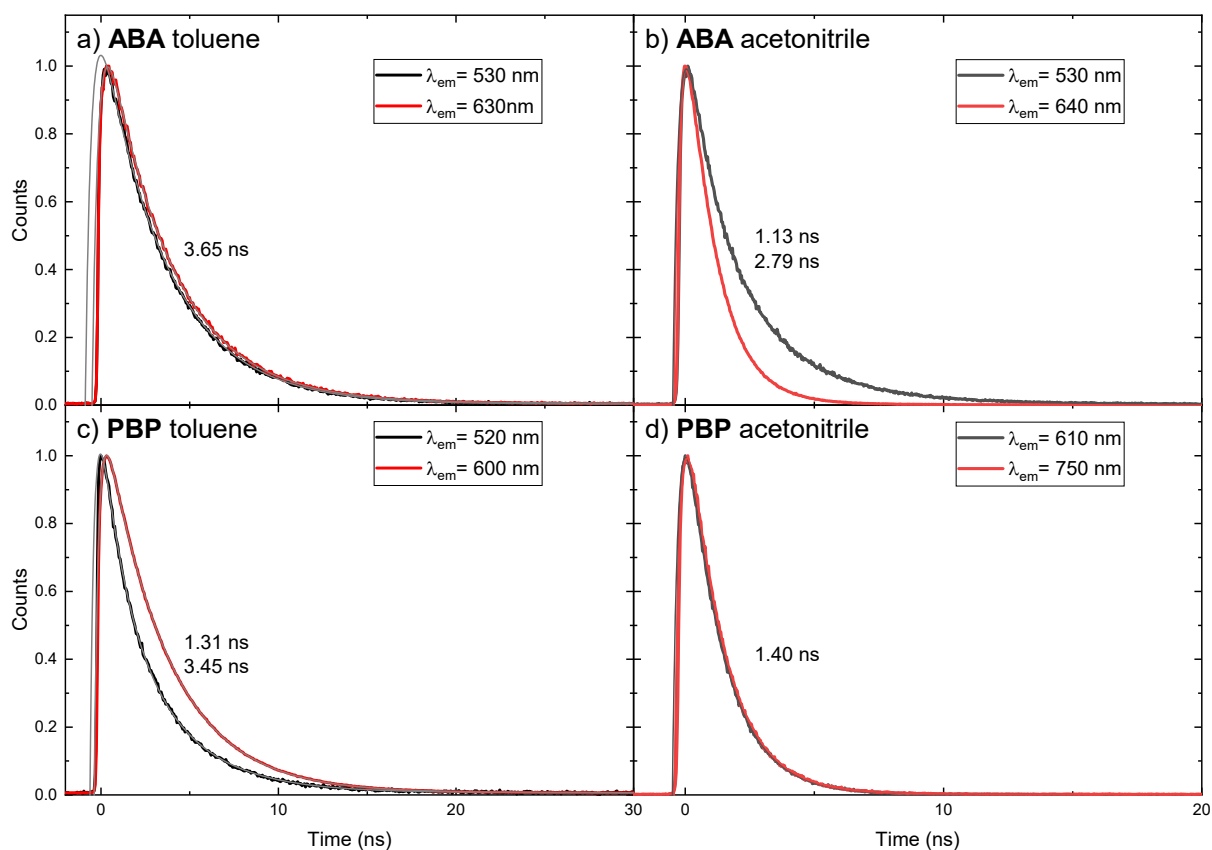


**Figure S14.** Time-resolved photoluminescence decays ( $\lambda_{exc} = 447$  nm) in a) **ABA** (19  $\mu$ M) and c) **PBP** (17  $\mu$ M) in toluene, and b) **ABA** and d) **PBP** in acetonitrile. Global tail fit (i.e. fixed lifetimes for the different emission wavelengths).

## 6. Computational details

Quantum chemical calculations were performed using M062X/6-31G(d) approach, which proved its efficacy in TD-DFT studies of large BODIPY systems.<sup>3</sup> UV-Vis absorption spectra were simulated using a superior Pople basis set (M062X/6-311G(2d,p)+ method). B3LYP and its range-separated analogue CAM-B3LYP functionals<sup>4</sup> were used for comparison. Polarizable continuum model (PCM) was used in all the cases.<sup>5</sup> All calculations were done using Gaussian 16 program package.<sup>6</sup>

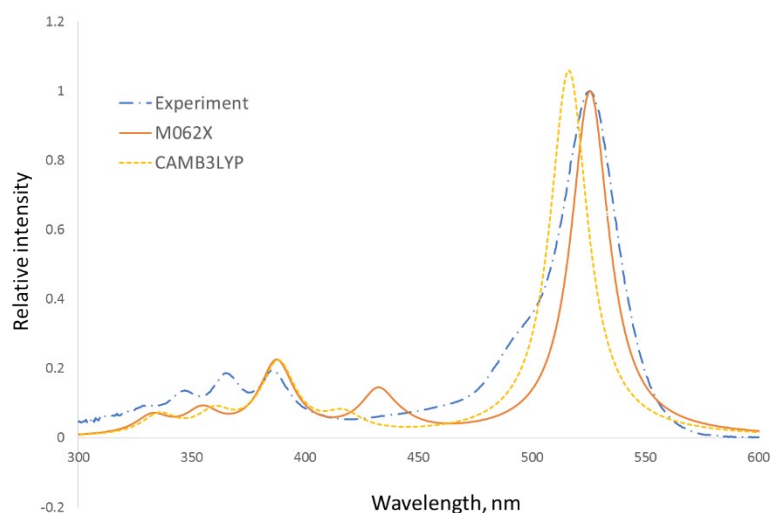


**Figure S15.** Comparison of the experimental and simulated spectra of **ABA** triad in acetonitrile. The 0-0 transition energy of the simulated spectra has been shifted by 74 nm (0.39 eV) and scaled by 1.08.

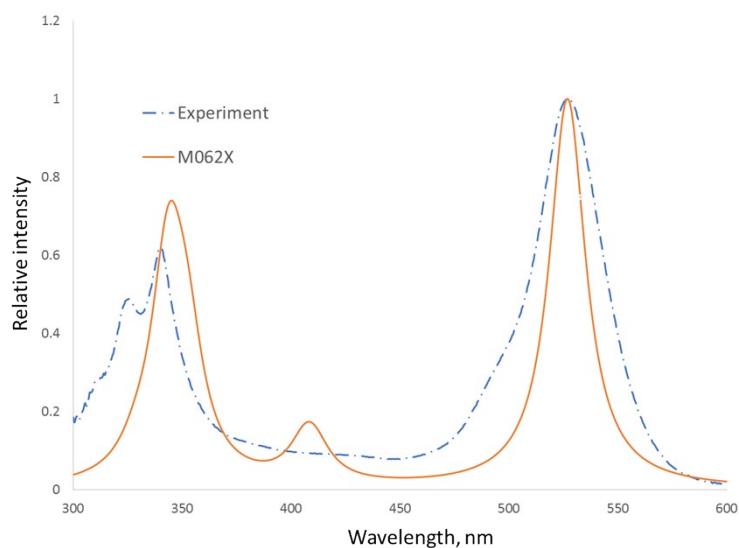


**Figure S16.** Comparison of the experimental and simulated spectra of **PBP** triad in ACN. The 0-0 transition energy of the simulated spectrum has been shifted by 72 nm (0.37 eV) and scaled by 1.247.

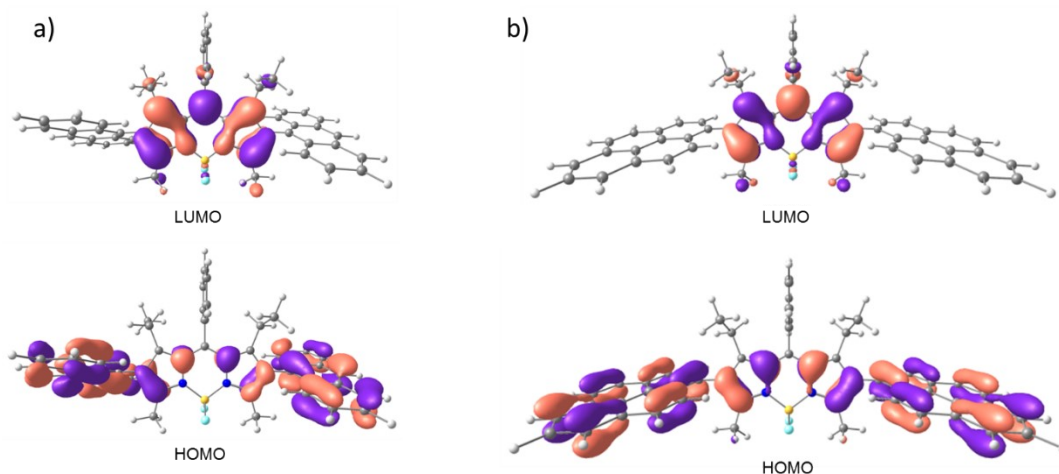


**Figure S17.** Frontier molecular  $\pi$ -type orbitals responsible for the optically bright  $S_0 \rightarrow S_1$  transition of the (a) **ABA** triad and (b) **PBP** triad calculated using M062X functional. Acetonitrile was used as a solvent.

### ABA excited states and geometry optimization

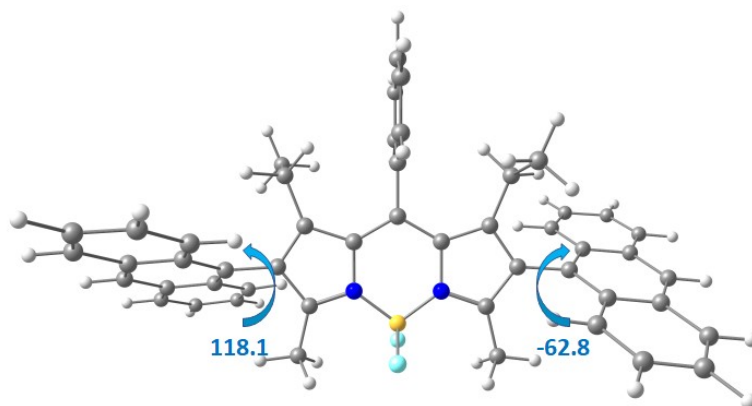


**Figure S18.** Optimized  $S_1$  geometries of **ABA** in acetonitrile according to the TDDFT M062X/6-31G(d) method.

Relative energy of the optimized  $S_1$  state (0-0 transition) equals 515 nm (2.41 eV) in ACN and 499 nm (2.48 eV) in toluene.

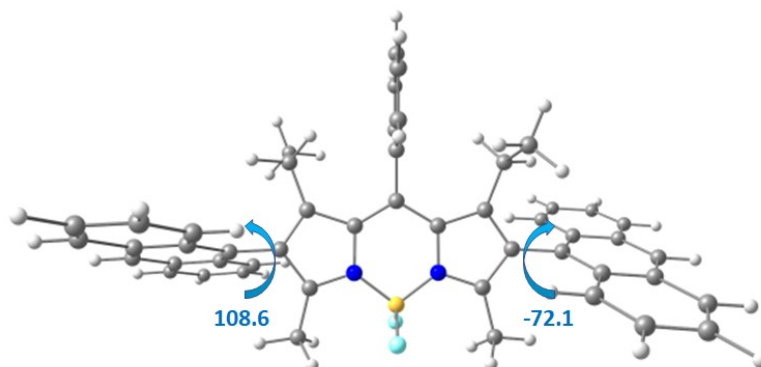


**Figure S19.** Optimized  $T_1$  geometry of the **ABA** triad in ACN according to the TDDFT M062X/6-31G(d) method.

Vertical  $T_1$  state energy in ACN equals 796 nm (1.558 eV), whereas  $T_2$  and  $T_3$  states are degenerate (for both vertical energies are equal to 556 nm, or 2.23 eV).  $T_4$  and  $T_5$  state vertical energies are equal to 423 nm (2.933 eV) and 407 nm (3.046 eV). In toluene, vertical  $T_1$  state energy equals 805 nm (1.54 eV), whereas  $T_2$  and  $T_3$  state energies are both equal to 557 nm (2.226 eV).  $T_4$  and  $T_5$  state vertical energies are equal to 423 nm (2.934 eV) and 406 nm (3.053 eV). Therefore, vertical energies of triplet states in ACN and toluene are almost identical, and the influence of solvent on  $T_n$  energy is minor.

### PBP excited states and geometry optimization

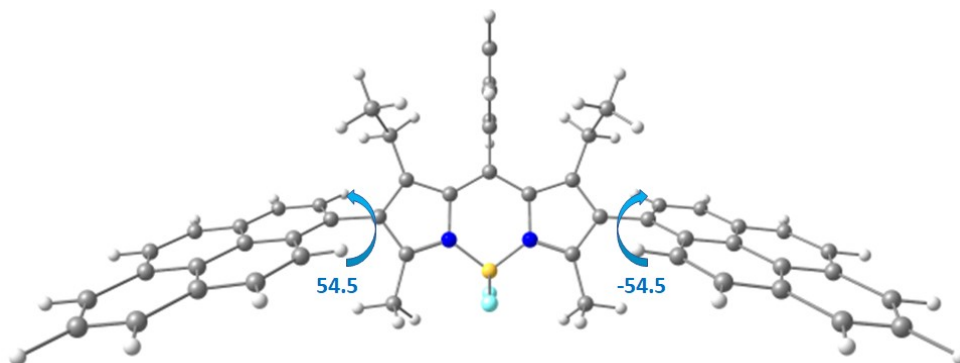


**Figure S20.** Optimized  $S_1$  geometries of the **PBP** triad in ACN according to M062X.

Relative energy of the optimized  $S_1$  state (0-0 transition) equals 517 nm (2.4 eV;  $f_{osc} = 1.328$ ) in ACN and 501 nm (2.47 eV;  $f_{osc} = 1.213$ ) in toluene.

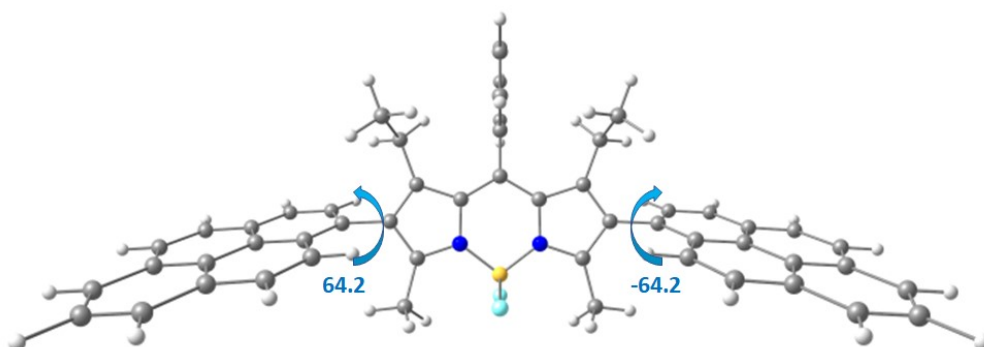


**Figure S21.** Optimized  $T_1$  state geometry of the **PBP** triad in ACN (TDDFT M062X/6-31G(d) method).

Vertical  $T_1$  state energy for **PBP** in ACN equals 800 nm (1.551 eV).  $T_2$  and  $T_3$  states are degenerate: both vertical energies are equal to 485 nm (2.555 eV). All three excited states  $T_1$ ,  $T_2$  and  $T_3$  are of  $^3\pi\pi^*$  nature, as well as  $S_1$  ( $^1\pi\pi^*$ ). For this reason, S-T transition is forbidden according to El-Sayed rule.  $T_4$  and  $T_5$  state vertical energies are equal to 422 nm (2.938 eV) and 399 nm (3.108 eV).

In toluene vertical  $T_1$  state energy equals 809 nm (1.532 eV), whereas  $T_2$  and  $T_3$  state energies are both equal to 485 nm (2.553 eV).  $T_4$  and  $T_5$  state vertical energies are equal to 422 nm (2.94 eV) and 399 nm (3.11 eV), respectively. Therefore, vertical energies of the triplet states in ACN and toluene are almost identical, and the difference between  $T_n$  energy in these solvents is minor or absent.

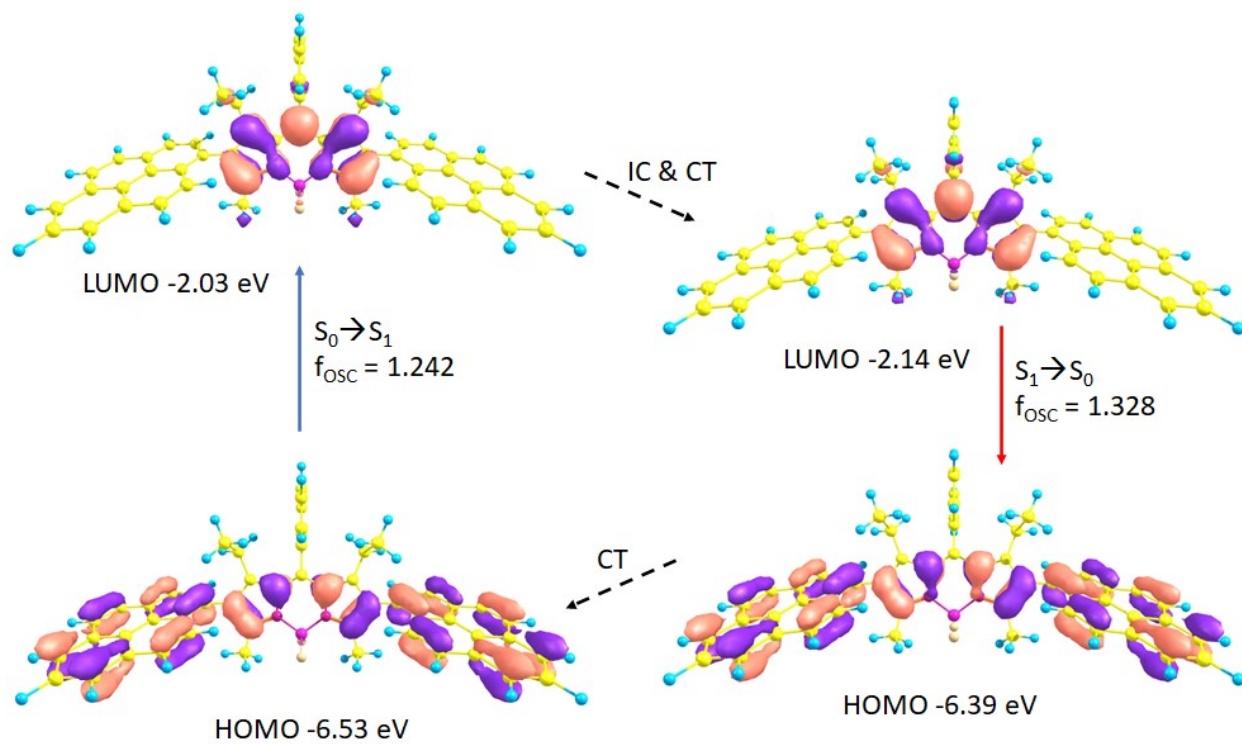


**Figure S22.** Rationalization of the large Stokes shift of the **PBP** triad: the geometry relaxation upon photoexcitation and molecular orbitals involved in the vertical absorption and emission.

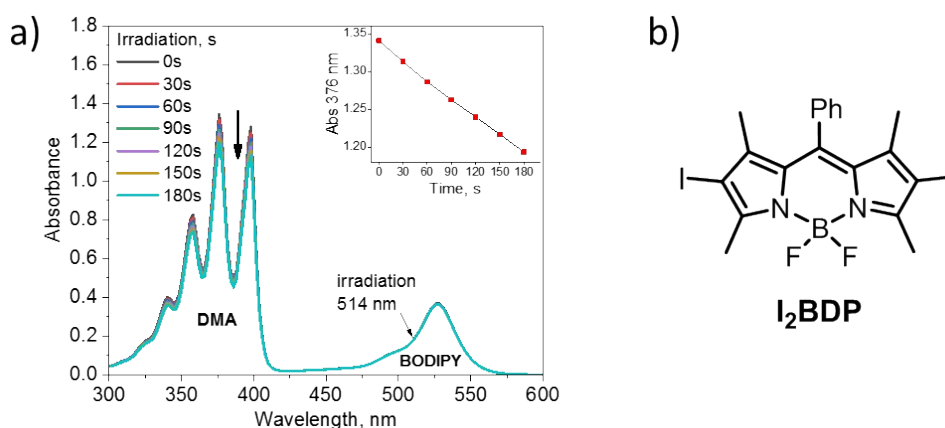
## 7. Singlet oxygen generation quantum yields measurements

The singlet oxygen quantum yield measurements were performed according to previously described method.<sup>7</sup> Solutions of the <sup>1</sup>O<sub>2</sub> trap, 1,9-dimethylantracene (DMA), with an optical density of around 1.4 in air-saturated solvent were employed. Corresponding BODIPY was added to the cuvette, and its absorbance was adjusted to 0.2-0.3 at the wavelength of irradiation. The solutions in the cuvette were irradiated with 514 nm laser light at a constant power density of 10 mW cm<sup>-2</sup>. The absorption spectra of the solutions were measured every 30 s. The slope of plots of absorbance of DMA at 376 nm vs. irradiation time for each photosensitizer was calculated.

Singlet oxygen quantum yields were calculated based on the equation:

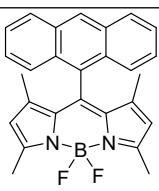
$$\Phi_{\Delta} = \Phi_{\Delta}^{ref} \times \frac{k}{k_{ref}} \times \frac{I_{abs}^{ref}}{I_{abs}} \quad (S1)$$

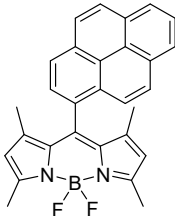
where  $\Phi_{\Delta}$  is the singlet oxygen quantum yield; the superscript *ref* stands for 2,6-diiodo-8-phenyl-1,3,5,7-tetramethylBODIPY (Figure S22b,  $\Phi_{\Delta} = 0.85$  in toluene)<sup>8</sup>; *k* is the slope of the curves of DMA absorption (376 nm) vs. irradiation time; *I*<sub>abs</sub> represents the absorption correction factor which is given by  $I = 1 - 10^{-OD}$  (OD is the optical density at 514 nm).



**Figure S23.** a) Photooxidation of 1,9-dimethylantracene in air-saturated THF solution containing ABA. Inset: dependence of the absorbance at 376 nm on the irradiation time. b) Reference photosensitizer I<sub>2</sub>BPD.

**Table S1.** Singlet oxygen quantum yields of reference BODIPY dyads in different solvents.

Compound	$\Phi_{\Delta}$				
	ACN	EtOH	THF	toluene	cyclohexane
	<b>0.767</b>	<b>0.667</b>	<b>0.465</b>	<b>0.067</b>	<b>0.059</b>

	<b>0.56</b>	<b>0.349</b>	<b>0.101</b>	<b>0.088</b>	<b>0.07</b>
---	-------------	--------------	--------------	--------------	-------------

## 8. Transient absorption spectroscopy

Transient absorption (TA) spectroscopy measurements were carried out using a home-built pump-probe setup. Two different configurations of the setup were used for either short delay, namely 100 fs to 8 ns experiments, or long delay, namely 1 ns to 300  $\mu$ s delays, as described below:

The output of a titanium:sapphire amplifier (Coherent LEGEND DUO, 4.5 mJ, 3 kHz, 100 fs) was split into three beams (2 mJ, 1 mJ, and 1.5 mJ). Two of them were used to separately pump two optical parametric amplifiers (OPA) (Light Conversion TOPAS Prime). The TOPAS 1 generates tunable pump pulses, while the TOPAS 2 generates signal (1300 nm) and idler (2000 nm) only. For measuring TA whole visible range, we used 1300 nm (signal) of TOPAS 2 to produce white-light super continuum from 350 to 1100 nm. For short delay TA measurements, we used the TOPAS 1 for producing pump pulses while the probe pathway length to the sample was kept constant at approximately 5 meters between the output of the TOPAS1 and the sample, the pump pathway length was varied between 5.12 and 2.6 m with a broadband retroreflector mounted on automated mechanical delay stage (Newport linear stage IMS600CCHA controlled by a Newport XPS motion controller), thereby generating delays between pump and probe from -400 ps to 8 ns.

For the 1 ns to 300  $\mu$ s delay (long delay) TA measurement, the same probe white-light supercontinuum as for the 100 fs to 8 ns delays was used. The excitation light (pump pulse) was provided by an actively Q-switched Nd:YVO<sub>4</sub> laser (InnoLas piccolo AOT) frequency-doubled (tripled) to provide pulses at 355 nm, and triggered by an electronic delay generator (Stanford Research Systems DG535), itself triggered by the TTL sync from the Legend DUO, allowing control of the delay between pump and probe with a jitter of roughly 100 ps.

Pump and probe beams were focused on the sample with the aid of proper optics. The transmitted fraction of the white light was guided to a custom-made prism spectrograph (Entwicklungsbüro Stresing) where it was dispersed by a prism onto a 512 pixel NMOS linear image sensor (Hamamatsu S8381-512). The probe pulse repetition rate was 3 kHz, while the excitation pulses were mechanically chopped to 1.5 kHz (100 fs to 8 ns delays) or directly generated at 1.5 kHz frequency (1 ns to 300  $\mu$ s delays), while the detector array was read out at 3 kHz. Adjacent diode readings corresponding to the transmission of the sample after excitation and in the absence of an excitation pulse were used to calculate  $\Delta T/T$ . Measurements were averaged over several thousand shots to obtain a good signal-to-noise ratio.

In the ps-ns TAS, samples were excited at 505 nm and in the ns-  $\mu$ s TAS, the excitation wavelength was 532 nm. In both experiments, we used the same solution in a 1 mm cuvette.

**Table S2.** Photophysical properties of **ABA** and **PBP** in acetonitrile and toluene (and Rose Bengal in methanol for reference). Singlet and triplet extinction ( $\epsilon_S$  and  $\epsilon_T$ , respectively) coefficients, intersystem crossing quantum yield ( $\Phi_{ISC}$ ).

Material / Solvent	Singlet decay/ CT generation (ps)	CT S decay/ triplet generation (ns)	$\tau_F$ (ns) $\lambda_{exc} = 447$ nm		Triplet Decay ( $\mu$ s)	$\Phi_{ISC}$ (%) by TAS			$\epsilon_{S,532nm}$ ( $M^{-1}cm^{-1}$ )	$\epsilon_T$ by Singlet Depletion Method ( $M^{-1}cm^{-1}$ )
						TAS	MCR-ALS (532 nm)	Relative Actinometry <sup>9</sup>		
<b>ABA</b> toluene	3.4	4	3.8		76	44	40	17-23	134961	7515
<b>PBP</b> toluene	2.7	3.9	1.31	3.45	109	36	26	17-23	81578	5539
Rose Bengal Methanol						76-90 from ref <sup>10</sup>			104700 from ref	7236 vs 6270 in ref <sup>11</sup>
<b>ABA</b> acetonitrile	2.0	2	1.13	2.79	1	23				
<b>PBP</b> acetonitrile	1.5	2.06	1.4		36	12.5				

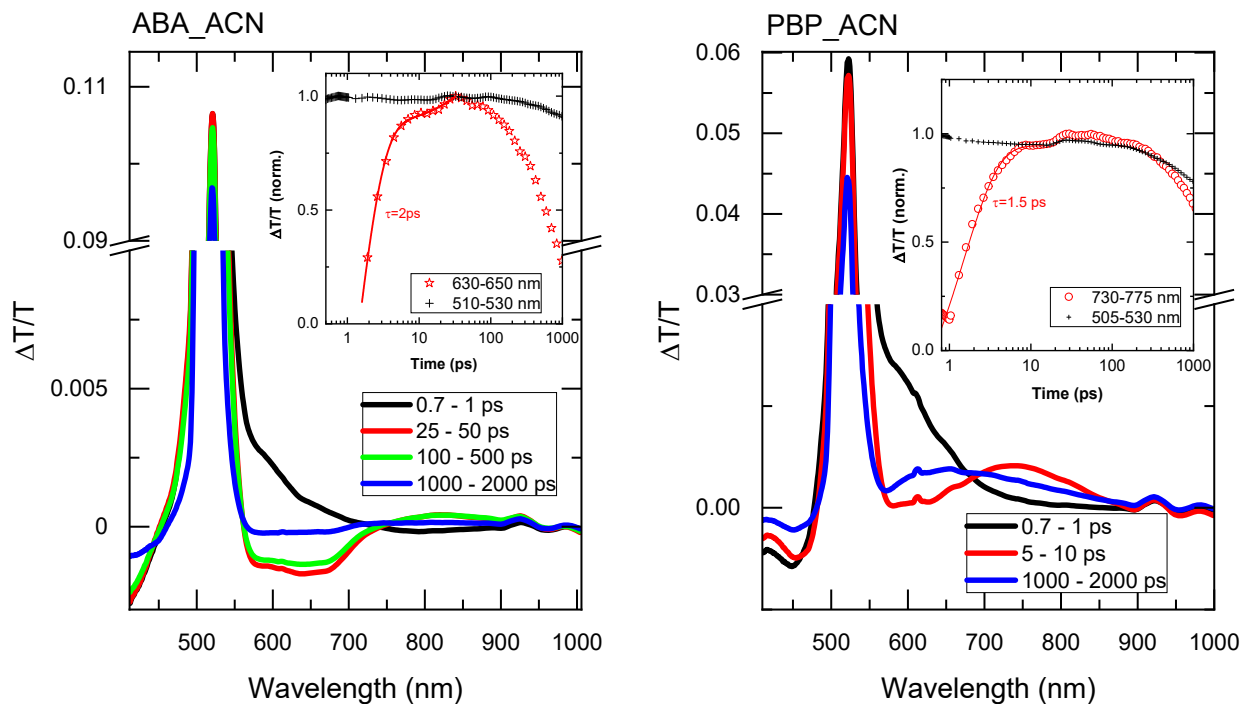


**Figure S24.** ps-ns TA spectra with kinetics of selected spectral region (inset) of ABA and PBP in acetonitrile.

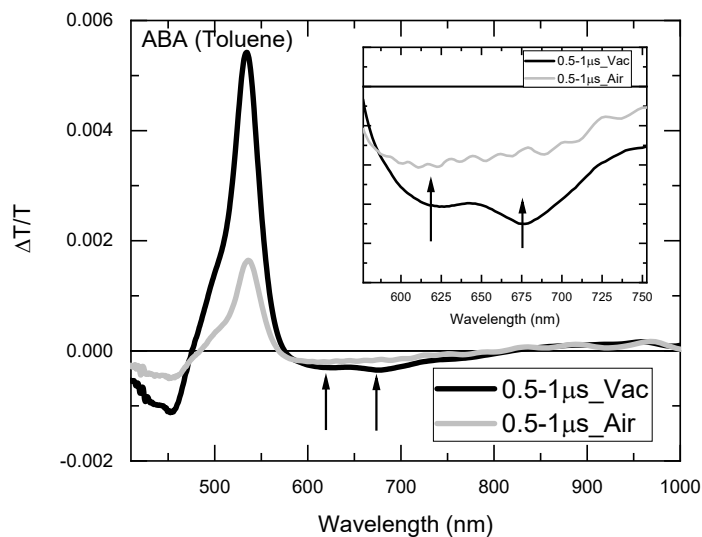


**Figure S25.** ns- $\mu$ s TA spectra of ABA in toluene in the presence of ambient air. The inset shows the zoomed-in region of triplet bands.

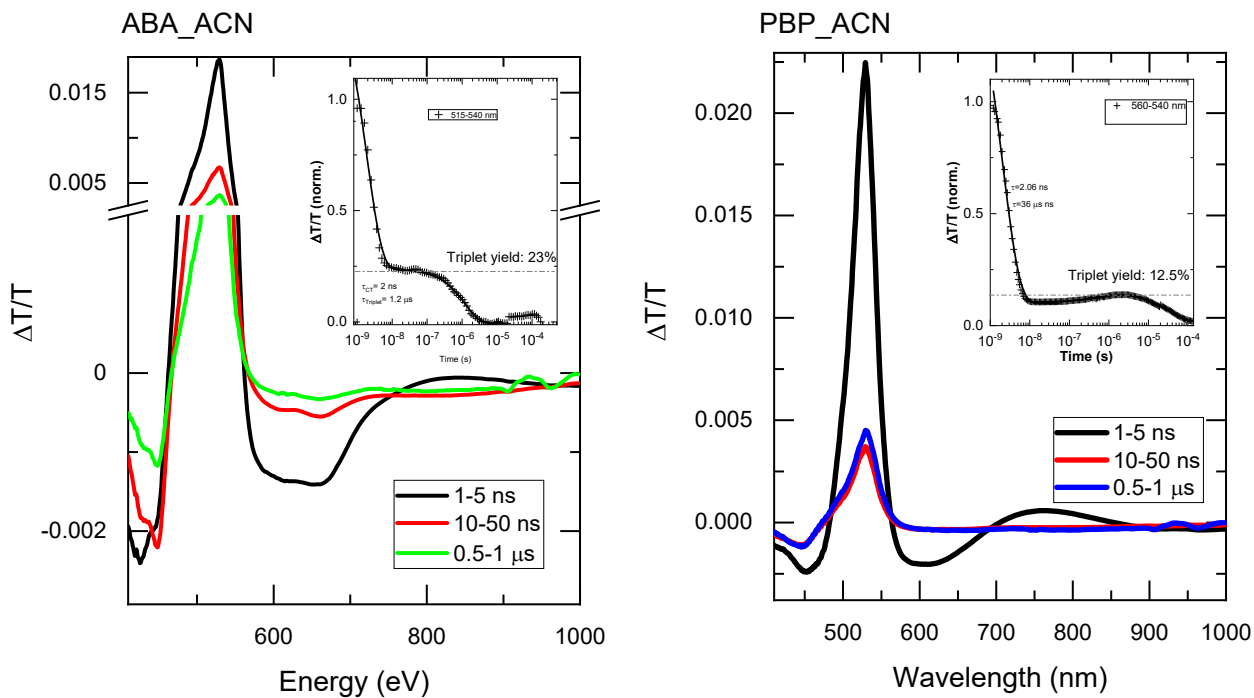


**Figure S26.** ns- $\mu$ s TA spectra with kinetics of selected spectral region (inset) of **ABA** and **PBP** in acetonitrile.

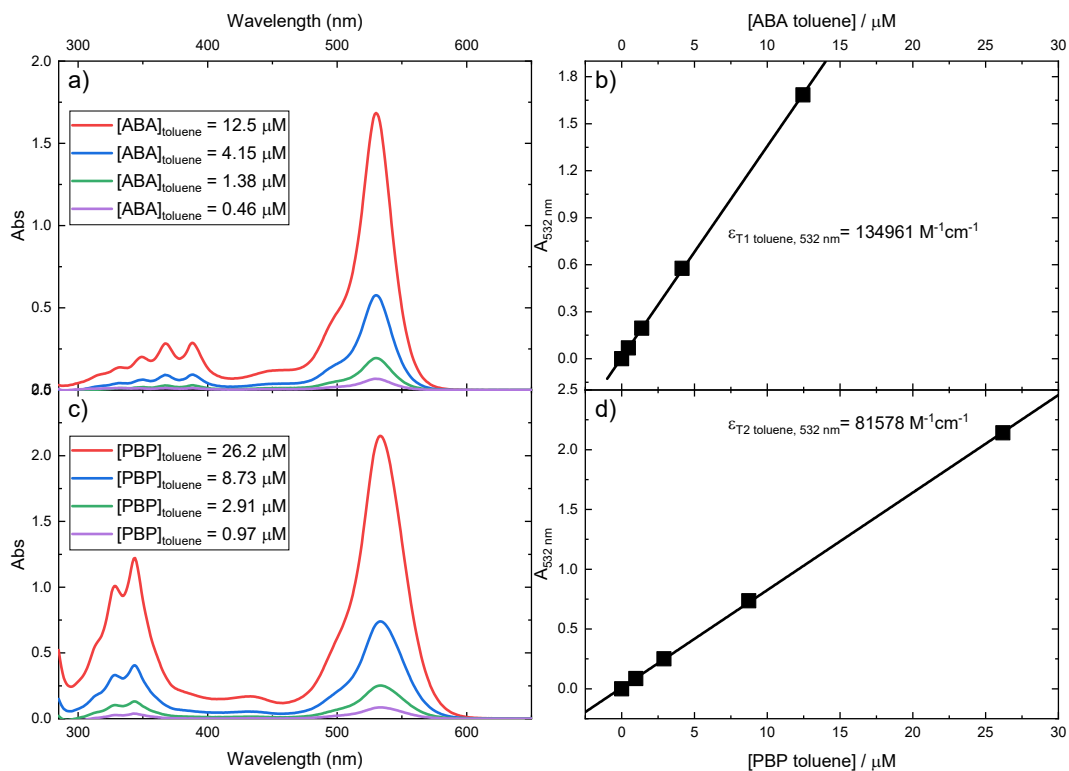


**Figure S27.** a), c) Absorption spectra and b), d) absorbance at 532 nm ( $A_{532 \text{ nm}}$ ) vs concentration for **ABA** and **PBP** in toluene, respectively.

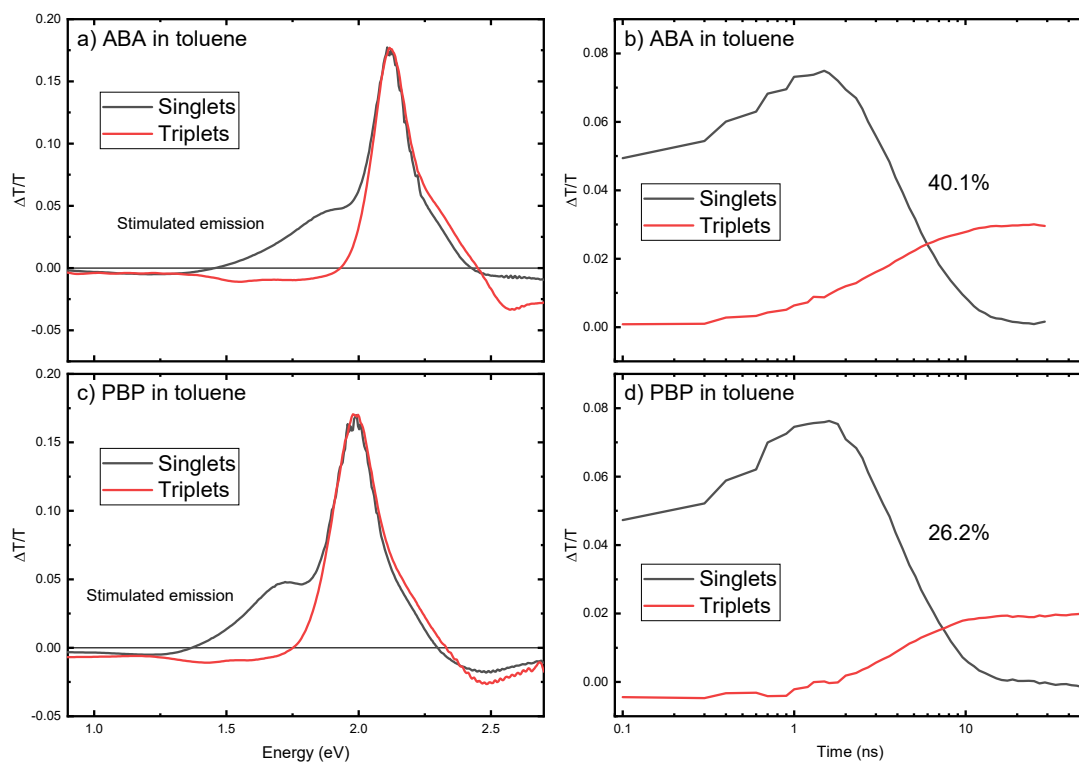


**Figure S28.** MCR-ALS ns-TAS  $\lambda_{\text{pump}} = 532 \text{ nm}$  for **ABA** and **PBP** in toluene with calculated  $\Phi_{\text{ISC}} = 40.1$  and 26.2% which decreases to 17-23% when taking into account their different  $\epsilon_{\text{T}}$  (obtained by the by Singlet Depletion Method – see Table S2), respectively.

## 9. Photopolymerizable glass preparation and holographic recording

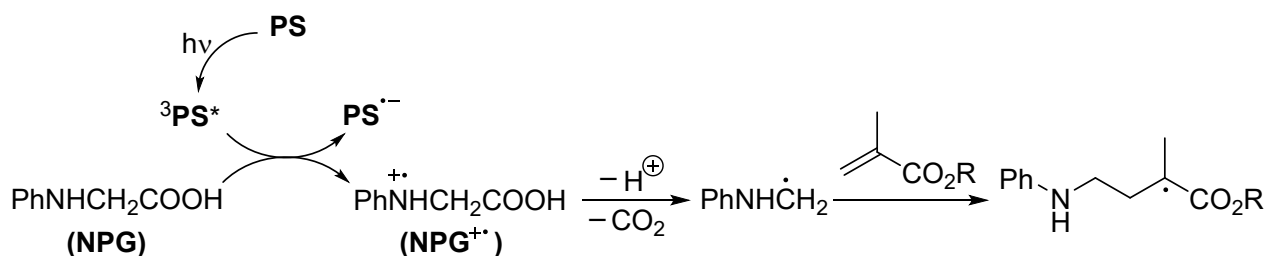
### 9.1. Synthesis of photopolymerizable glass (PG)

All chemicals used for the PG synthesis were purchased from Merk. Synthesis was performed following a previously published procedure.<sup>12</sup> 3-trimethoxysilylpropyl methacrylate (MAPTMS, 60.4 mmol) was mixed with 0.1 M aqueous nitric acid solution (HNO<sub>3</sub>, 44.4 mmol) and the resulting solution was stirred for 45 min. Zirconium complex was prepared by mixing zirconium (IV) propoxide (ZPO, 2.218 mmol) and methacrylic acid (MAA, 1.567 mmol), followed by stirring for 45 min. Then, MAPTMS/HNO<sub>3</sub> solution was added to ZPO/MAA solution and stirred for 10 min followed by addition of water (60.4 mmol). The resulting mixture was stirred further for 24 hours leading to the formation of the base of the sol gel. After stirring, (3-aminopropyl)triethoxysilane (APTES, 3.608 mmol) was added to achieve the concentration of 4.5% w/w. At the same time, **ABA** or **I<sub>2</sub>BDP** sensitizer (0.0154 mmol) and *N*-phenyl glycine (NPG, 0.861 mmol) were added. The resulting formulation was stirred for 10 hours in a dark room at ambient conditions.

### 9.2 Photosensitive glass layer preparation

The PG layers were prepared by a drop casting method using 0.7 ml of sol on the levelled glass slide (38 × 25 mm<sup>2</sup>, 1 mm thickness). After coating, the samples were cured at 100 °C for 45 min in the oven (Binder, model ED56) to complete gelation and achieve fully cured layers suitable for holographic recording.

### 9.3 Photoinitiation mechanism



**Scheme S1.** The mechanism of photosensitized decomposition of NPG described in previous works.<sup>13</sup> PS - photosensitizer, <sup>3</sup>PS\* - triplet excited state, PS<sup>•-</sup> - radical anion.

### 9.4 Diffraction efficiency measurements

The holographic recording of volume phase transmission gratings was carried out using the set-up presented in Figure S28. Unslanted gratings with a spatial frequency of 800 lines mm<sup>-1</sup> were recorded in layers with thickness of 220-260 μm using the optimum total recording intensity of 58 mW cm<sup>-2</sup>. During holographic patterning, the PG layers were exposed to two beams of 532 nm wavelength obtained by splitting a Nd:YVO<sub>4</sub> laser beam. The angle of incidence of the recording beams (θ) was 12.3° with respect to the normal to the surface of the sample.

The dynamic of the grating formation was monitored by recording the real-time diffraction efficiency growth curve during holographic patterning. A low intensity (1.8 mW cm<sup>-2</sup>) 633 nm beam from a He-Ne laser was employed as a probe beam for both real-time diffraction efficiency and Bragg selectivity curve measurements (Figure S28). The laser beam intensity was monitored using an optical power meter (Newport, model 843-R) and the acquired data were transferred to a computer. The diffraction efficiency (η) of the transmission gratings was calculated as the ratio of the first-order diffracted beam intensity (I<sub>1</sub>) and incident beam intensity (I<sub>in</sub>)

$$\eta = \frac{I_1}{I_{in}} \times 100\% . \quad (\text{S2})$$

To measure the Bragg selectivity curves, the sample was mounted on a rotation stage, which was computer controlled via a motion controller (Newport ESP300). Experimental Bragg selectivity curves were used to estimate the layer thickness ( $d$ ) utilising the following Coupled-Wave theory equation<sup>14</sup>

$$\Delta\theta_{FWHM} = \frac{\Lambda}{d}, \quad (S3)$$

where  $\Delta\theta_{FWHM}$  is the full angular bandwidths at the half of the maximum of the diffraction efficiency,  $\Lambda$  – spatial period.

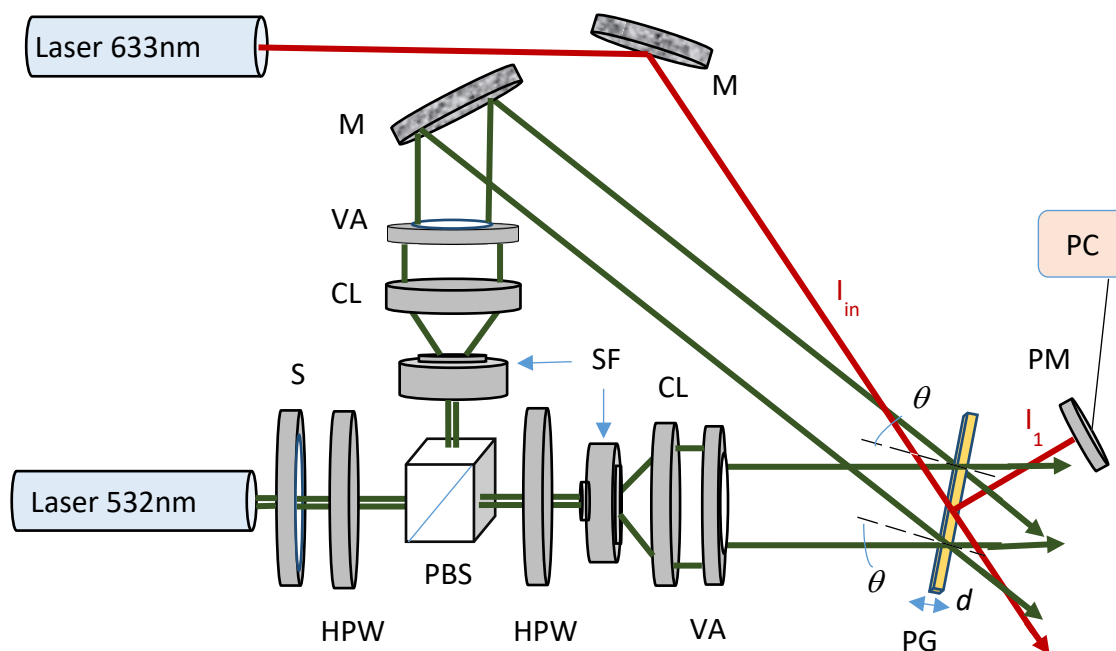


**Figure S29.** Schematic representation of the experimental set up for the holographic recording of transmission gratings with the spatial frequency of about  $800 \text{ l mm}^{-1}$ . S – electronic shutter, HWP - half-wave plate, PBS - polarising beam splitter, SF – spatial filter, CL – collimator, VA - variable aperture, PG – photopolymerisable glass, M – mirror, PM - power meter, PC – computer.

### 9.5 Coupled-wave theory analysis for volume holographic gratings

A holographic grating can be classified as a volume grating, if the thickness ( $d$ ) of the recorded hologram is substantial in comparison with its spatial period ( $\Lambda$ ). This classification can be quantified by the Klein-Cook  $Q$ -parameter, where a volume grating has a  $Q$ -parameter value higher than ten<sup>15</sup>

$$Q = \frac{2\pi\lambda d}{n\Lambda^2}, \quad (S4)$$

where  $\lambda$  is a wavelength of the recording light,  $n$  is the average refractive index of the medium. Quantitative analysis of volume phase gratings is carried out using the Kogelnik's Coupled-Wave theory.<sup>13</sup> According to the coupled-wave theory, refractive index modulation ( $\Delta n$ ) achieved during holographic recording in transmission mode can be determined using the following equation

$$\Delta n = \frac{\lambda \cos\theta \sin^{-1}(\sqrt{\eta})}{\pi d}, \quad (S5)$$

where  $\lambda$  is the wavelength of the reconstructing beam,  $\theta$  is the Bragg angle inside the medium for the reconstructing wavelength and  $\eta$  is the diffraction efficiency.

In accordance with the coupled wave theory, the diffraction efficiency of a volume phase transmission grating is determined by

$$\eta = \frac{\sin^2 \sqrt{(\xi^2 + \nu^2)}}{1 + \xi^2 / \nu^2}. \quad (\text{S6})$$

The parameter  $\nu$  defines the maximum diffraction efficiency at Bragg incidence, whereas the parameter  $\xi$  describes deviation from the Bragg condition due to the angular and wavelength deviations. At Bragg incidence  $\xi = 0$  and the maximum diffraction efficiency is determined

$$\eta = \sin^2 \nu. \quad (\text{S7})$$

The parameter  $\nu$  can be written as

$$\nu = \frac{\pi \Delta n d}{\lambda \cos \theta}, \quad (\text{S8})$$

where  $\lambda$  is the wavelength of the reconstructing beam. At non-Bragg incidence, the parameter  $\xi$  is described

$$\xi = \Delta\theta \frac{kd}{2}, \quad (\text{S9})$$

where  $\Delta\theta$  is the deviation from Bragg angle,  $k$  is the wave vector of the grating and its magnitude is determined as  $2\pi/\lambda$ .

## 9.6 Calculation of the photosensitivity of holographic recording materials

Photosensitivity ( $S$ ) of the holographic recording material is defined as the ratio between the square root of the diffraction efficiency and the product of the exposure energy ( $E$ ) and the visibility ( $V$ )<sup>16</sup>

$$\sqrt{\eta} = SEV, \quad (\text{S10})$$

where visibility is defined by the ratio of the recording beam intensities ( $R$ )

$$V = \frac{2R^{-1/2}}{(1+R)}. \quad (\text{S11})$$

In the current experimental conditions, the holographic recording is performed using two beams with equal intensity which provides  $R = 1$ . Thus, calculation of  $S$  is carried out by plotting  $\sqrt{\eta}$  versus  $E$  obtained as the product of the total recording intensity and recording time (Figure S29). The slope of the straight-line portion of the graph corresponds to  $E$  ( $\text{J}^{-1} \text{cm}^2$ ).

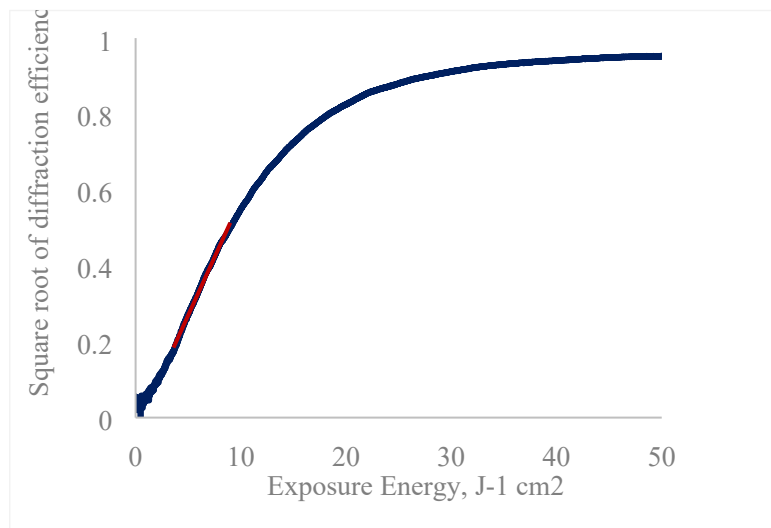


**Figure S30.** Square root of the diffraction efficiency growth curve of the photopolymerizable glass containing **ABA** as a photosensitizer. The slope of the linear part (marked in red) corresponds to the exposure sensitivity of PG-**ABA**, which is equal to  $6.1 \times 10^{-2} \text{ J}^{-1} \text{ cm}^2$ .

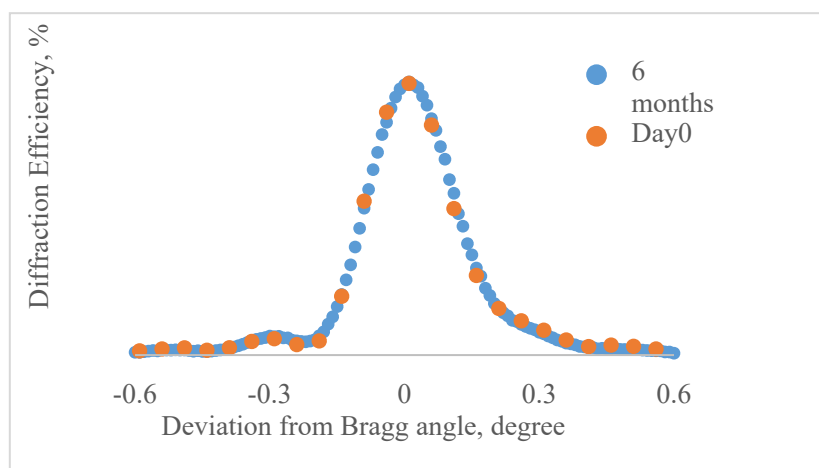


**Figure S31.** Bragg selectivity curves of the grating recorded in PG-**ABA** show stable diffraction efficiency after 6 months.

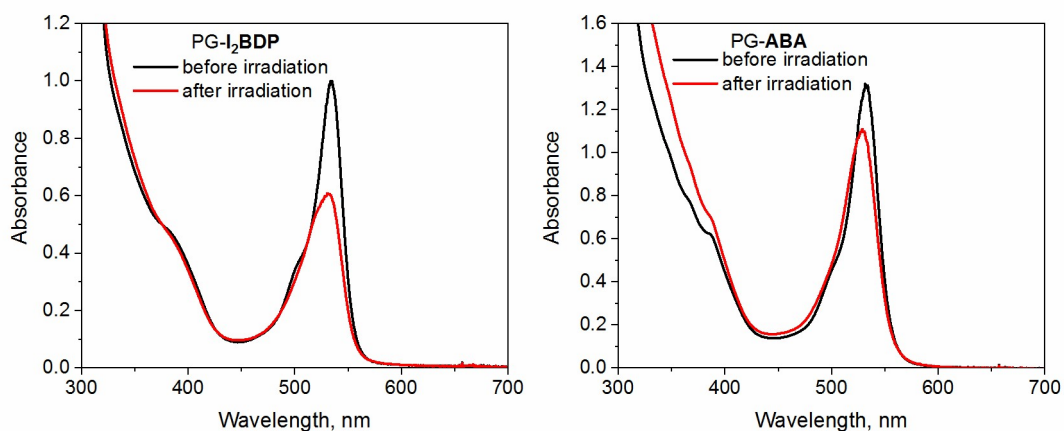


**Figure S32.** UV-Vis absorption spectra of PG-**ABA** and PG-**I<sub>2</sub>BDP** layers (260  $\mu\text{m}$  thickness) before (black line) and after (red line) holographic recording with 532 nm laser.

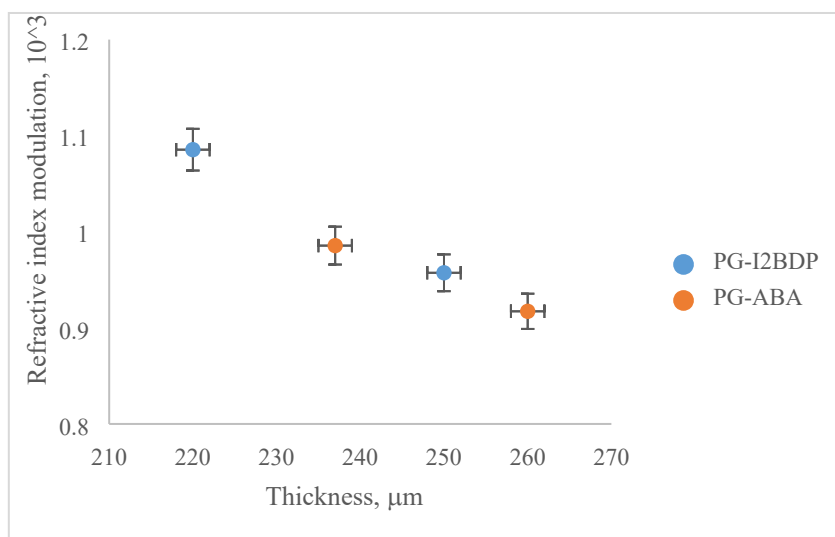


**Figure S33.** Refractive index modulation achieved in PG-ABA and PG-I<sub>2</sub>BDP layers with different thickness.

## 10. References

- <sup>1</sup> J.R. Lakowicz, Principles of Fluorescence Spectroscopy, 2nd Ed., Kluwer Academic/Plenum Publishers, New York, London, Moscow, Dordrecht, 1999.
- <sup>2</sup> L. Gutiérrez-Arzaluz, G.H. Ahmed, H. Yang, S. Shikin, O.M. Bakr, A.V. Malko, O.F. Mohammed, *J. Phys. Chem. A*, **2020**, *124*, 4855.
- <sup>3</sup> S. Chibani, A. Charaf-Eddin, B. Mennucci, B. Le Guennic, D. Jacquemin, *J. Chem. Theory Comput.*, **2014**, *10*, 805.
- <sup>4</sup> (a) Y. Chen, J. Zhao, H. Guo, L. Xie, *J. Org. Chem.*, **2012**, *77*, 2192; (b) A. Rose, S. V Kumar, S. Swavey, J. Erb, *Comput. Theor. Chem.*, **2017**, *1118*, 107; (c) I.K. Petrushenko, K.B. Petrushenko, *Spectrochim. Acta. A. Mol. Biomol. Spectrosc.*, **2019**, *206*, 498.
- <sup>5</sup> J. Tomasi, B. Mennucci, R. Cammi, *Chem. Rev.*, **2005**, *105*, 2999.
- <sup>6</sup> D. J. Frisch, M. J.; Trucks, G. W.; Schlegel, H. B.; Scuseria, G. E.; Robb, M. A.; Cheeseman, J. R.; Scalmani, G.; Barone, V.; Petersson, G. A.; Nakatsuji, H.; Li, X.; Caricato, M.; Marenich, A. V.; Bloino, J.; Janesko, B. G.; Gomperts, R.; Mennucci, B.; Hratch, M. J. Frisch, G. W. Trucks, H. B. Schlegel, G. E. Scuseria, M. A. Robb, J. R. Cheeseman, G. Scalmani, V. Barone, G. A. Petersson, H. Nakatsuji, X. Li, M. Caricato, A. V. Marenich, J. Bloino, B. G. Janesko, R. Gomperts, B. Mennucci, H. P. Hratchian, J. V. Ortiz, A. F. Izmaylov, J. L. Sonnenberg, D. Williams-Young, F. Ding, F. Lipparini, F. Egidi, J. Goings, B. Peng, A. Petrone, T. Henderson, D. Ranasinghe, V. G. Zakrzewski, J. Gao, N. Rega, G. Zheng, W. Liang, M. Hada, M. Ehara, K. Toyota, R. Fukuda, J. Hasegawa, M. Ishida, T. Nakajima, Y. Honda, O. Kitao, H. Nakai, T. Vreven, K. Throssell, J. A. Montgomery Jr., J. E. Peralta, F. Ogliaro, M. J. Bearpark, J. J. Heyd, E. N. Brothers, K. N. Kudin, V. N. Staroverov, T. A. Keith, R. Kobayashi, J. Normand, K. Raghavachari, A. P. Rendell, J. C. Burant, S. S. Iyengar, J. Tomasi, M. Cossi, J. M. Millam, M. Klene, C. Adamo, R. Cammi, J. W. Ochterski, R. L. Martin, K. Morokuma, O. Farkas, J. B. Foresman, D. J. Fox, 2016, Gaussian 16, Revision C.01, Gaussian, Inc., Wallin.
- <sup>7</sup> L. Gou, C. N. Coretsopoulos and A. B. Scranton, *J. Polym. Sci. Part A Polym. Chem.*, **2004**, *42*, 1285.
- <sup>8</sup> A.A. Buglak, A. Charisiadis, A. Sheehan, C.J. Kingsbury, M.O. Senge, M.A. Filatov, *Chem. Eur. J.*, **2021**, *27*, 9934.
- <sup>9</sup> (a) J. S. de Melo, J. Pina, F. B. Dias and A. L. Maçanita, in Applied Photochemistry, ed. R. C. Evans, P. Douglas and H. D. Burrows, Springer, 2013, ch. 15, p. 533.; (b) I. Carmichael, G.L. Hug, *J. Phys. Chem. Ref. Data*, **1986**, *15*, 1.
- <sup>10</sup> L. Ludvíková, P. Friš, D. Heger, P. Šebej, J. Wirz, P. Klán, *Phys. Chem. Chem. Phys.*, **2016**, *18*, 16266.
- <sup>11</sup> P. Murasecco-Suardi, E. Gassmann, A.M. Braun, E. Oliveros, *Helv. Chim. Acta*, **1987**, *70*, 1760.
- <sup>12</sup> T. Mikulchyk, M. Oubaha, A. Kaworek, B. Duffy, M. Lunzer, A. Ovsianikov, S. E-Gul, I. Naydenova, D. Cody, *Adv. Opt. Mater.*, **2022**, *10*, 2102089.
- <sup>13</sup> S. Ikeda, S. Murata, K. Ishii, H. Hamaguchi, *Chem. Lett.*, **1999**, 1009.
- <sup>14</sup> H. Kogelnik, *Bell Syst. Tech. J.*, **1969**, *48*, 2909.
- <sup>15</sup> P. Phariseau, in *Proc. Indian Acad. Sci. - Sect. A*, **1956**, 44.
- <sup>16</sup> P. Hariharan, Optical Holography: Principles, Techniques and Applications Cambridge U. Press, Cambridge, UK, 1984